The Astrophysical Journal, 894:71 (20pp), 2020 May 1 https://doi.org/10.3847/1538-4357/ab879d

A Broadband X-Ray Study of a Sample of AGNs with [O III] Measured Inclinations

X. Zhao[1], S. Marchesi[1,2], M. Ajello[1], M. Baloković[3,4], and T. Fischer[5]
[1] Department of Physics & Astronomy, Clemson University, Clemson, SC 29634, USA
[2] INAF-Osservatorio Astronomico di Bologna, Via Piero Gobetti, 93/3, I-40129, Bologna, Italy
[3] Center for Astrophysics, Harvard & Smithsonian, 60 Garden Street, Cambridge, MA 02138, USA
[4] Black hole Initiative at Harvard University, 20 Garden Street, Cambridge, MA 02138, USA
[5] Astrometry Department, United States Naval Observatory, 3450 Massachusetts Avenue, NW, Washington, DC 20392, USA
Received 2019 November 1; revised 2020 March 26; accepted 2020 April 6; published 2020 May 7

Abstract

In modeling the X-ray spectra of active galactic nuclei (AGNs), the inclination angle is a parameter that can play an important role in analyzing the X-ray spectra of AGNs, but it has never been studied in detail. We present a broadband X-ray spectral analysis of the joint Nuclear Spectroscopic Telescope Array-XMM-Newton observations of 13 sources with [O III] measured inclinations determined by Fischer et al. By freezing the inclination angles at the [O III] measured values when modeling the observations, the spectra are well fitted, and the geometrical properties of the obscuring structure of the AGNs are slightly better constrained than those fitted when the inclination angles are left free to vary. We also test if one could freeze the inclinations at other specific angles in fitting the AGN X-ray spectra as has been commonly done in the literature. We find that one should always let the inclination angle be free to vary in modeling the X-ray spectra of AGNs, while fixing the inclination angle at [O III] measured values and fixing the inclination angle at 60° also present correct fits of the sources in our sample. Correlations between the covering factor and the average column density of the obscuring torus with respect to the Eddington ratio are also measured, suggesting that the distribution of the material in the obscuring torus is regulated by the Eddington ratio, which is in agreement with previous studies. In addition, no geometrical correlation is found between the narrow line region of the AGN and the obscuring torus, suggesting that the geometry might be more complex than what is assumed in the simplistic unified model.

Unified Astronomy Thesaurus concepts: Active galactic nuclei (16)

1. Introduction

It is commonly accepted that the main structure of an active galactic nucleus (AGN) is composed of a supermassive black hole (SMBH; $M_{\rm BH} \approx 10^{6-9.5} M_{\odot}$) at the center of the AGN, an accretion disk surrounding the SMBH, a subparsec-scale dust-free region known as the broad line region, where broad lines with FWHM $> 2000\,{\rm km\,s^{-1}}$ are observed in optical, a parsec-scale toroidal structure composed of gas and dust obscuring the emission from the center engine of the AGN, and a broaden structure ($\sim$10 pc to $\sim$1 kpc), namely, the narrow line region (NLR; FWHM $< 1000\,{\rm km\,s^{-1}}$; see, e.g., Netzer 2015; Almeida & Ricci 2017; Hickox & Alexander 2018, for recent reviews). AGNs are optically classified as type 1 or type 2 AGNs if the broad-emission lines can be observed in their optical spectra or not. According to the AGN unified model (Antonucci 1993; Urry & Padovani 1995), type 2 AGNs are the AGNs whose line of sight between the central engine and the observer passes the dusty toroidal structure, and type 1 AGNs are those whose line of sight does not intercept the torus. Furthermore, the torus is also thought to play an important role in the coevolution of the SMBH and the host galaxy (see, e.g., Kormendy & Ho 2013; Heckman & Best 2014). Therefore, putting strong constraints on the physical and geometrical properties of the toroidal structure is essential to understand the basics of AGNs.

Observing the X-ray emission from AGNs is a powerful method to probe their obscuring toroidal structure. The intrinsic X-ray emission produced by the central engine of the AGN is reprocessed by the obscuring torus: studying this reprocessed X-ray emission can then provide an abundance of information about the properties of the torus. One of the ubiquitous signatures of this reprocessed component is the fluorescent Fe Kα line at 6.4 keV, originating from the outer side of the accretion disk or the inner edge of the torus (see, e.g., Fabian et al. 2000; Reynolds & Nowak 2003; Yaqoob & Padmanabhan 2004, for reviews), which could provide significant information on both the physics and dynamics of the circumnuclear materials (Leahy & Creighton 1993; Reynolds 1999; Matt 2002; Shu et al. 2010; Ricci et al. 2014). XMM-Newton is the best instrument to study such a signature in terms of both effective area between 0.3 and 10 keV and spectral resolution. Indeed, many studies have been done on the properties of the torus utilizing XMM-Newton (e.g., Georgantopoulos et al. 2013; LaMassa et al. 2014). Another spectral signature of the reprocessed component, which is particularly prominent in heavily obscured AGNs (i.e., sources with column density $N_{\rm H} \geqslant 10^{24}\,{\rm cm^{-2}}$), is the so-called "Compton hump" peaked at 10–40 keV (see, e.g., Ghisellini et al. 1994; Krolik et al. 1994). Thus, the proper characterization of heavily obscured AGNs, which are thought to be $\sim$20%–30% of all AGNs according to different CXB synthesis models predictions (Alexander et al. 2003; Gandhi & Fabian 2003; Gilli et al. 2007; Treister et al. 2009; Ueda et al. 2014; Ananna et al. 2019), requires an X-ray telescope sensitive above 10 keV. The launch of the Nuclear Spectroscopic Telescope Array (NuSTAR; Harrison et al. 2013), which is the first instrument to focus on X-ray at energy $>$10 keV and provides a two orders of magnitude better sensitivity than previous telescopes (e.g., INTEGRAL and Swift-BAT; Winkler et al. 2003; Barthelmy et al. 2005) at $\sim$10–50 keV, allowed us to characterize the physical properties of heavily obscured AGNs with unprecedented accuracy (e.g., Baloković et al. 2014; Puccetti et al. 2014; Annuar et al. 2015; Ursini et al. 2015, 2018; Koss et al. 2016; Marchesi et al. 2017). Therefore, the combination of NuSTAR

and XMM-Newton provides one of the best methods to study the properties of a heterogeneous AGN population in the local universe (see, e.g., Marinucci et al. 2014; Fürst et al. 2016; Ursini et al. 2016; la Caria et al. 2019; Marchesi et al. 2019; Walton et al. 2019; Zhao et al. 2019a, 2019b).

In recent years, several tori models based on Monte Carlo simulations have been developed to characterize the X-ray spectra of AGNs (Matt & Fabian 1994; Ikeda et al. 2009; Murphy & Yaqoob 2009; Brightman & Nandra 2011; Paltani & Ricci 2017; Baloković et al. 2018; Tanimoto et al. 2019). Different models adopt different assumptions on the geometry of the torus; e.g., Murphy & Yaqoob (2009), Liu & Li (2014), and Furui et al. (2016) assume a half-opening angle of the torus fixed at $\theta_{\rm h.o.} = 60^\circ$ but a variable inclination angle of the torus ($\theta_{\rm obs}$). Ikeda et al. (2009), Brightman & Nandra (2011), Paltani & Ricci (2017), Baloković et al. (2018), and Tanimoto et al. (2019) assume a flexible half-opening angle of the torus and a variable inclination angle. Given the intrinsic complexity of these models and the multiple free parameters involved, applying them in full capability is still difficult especially with low-quality X-ray spectra: in particular, the inclination angle of the AGN is hard to constrain. Thus, it is common to freeze $\theta_{\rm obs}$ in the spectral analysis process (see, e.g., Yaqoob 2012; Kawamuro et al. 2013; Brightman et al. 2015; Koss et al. 2015, 2016; Yaqoob et al. 2015; Ricci et al. 2016; Gandhi et al. 2017; Marchesi et al. 2018). However, the validity of the method of freezing the inclination angle has not yet been studied in a systematic way. The studies on the NLRs of AGNs can provide us with a method to overcome this issue by measuring the inclinations of the AGNs by mapping the kinematics of their NLRs. Fischer et al. (2013) successfully measured the inclinations of the NRLs and, thus, the torus with respect to our line of sight in 17 AGNs by fitting the radial outflow dominated NLR kinematics resolved by Hubble Space Telescope (HST) [O III] imaging and Space Telescope Imaging Spectrograph (STIS) with a biconical outflow model.

In this work, we study the role of inclination angle in fitting the AGN X-ray spectra by comparing the best-fit results obtained when the broad X-ray spectra of the sources in the sample of Fischer et al. (2013) are fitted with the inclination angle being (i) left free to vary, (ii) fixed at [O III] measured values, (iii) fixed at 60°, and (iv) fixed at 87°. The paper is organized as follows. In Section 2, we report the sample selection rules and the NuSTAR, XMM-Newton, and Chandra data reduction process. In Section 3, we describe the model used to fit the broadband X-ray spectra, the fitting procedure, and best-fit results of each source in our sample. In Section 4, we discuss how fixing the inclination angle affects the broadband X-ray spectral analysis of AGNs, and we study the geometrical properties of the AGNs in both X-ray and optical. All reported uncertainties on spectral parameters are at the 90% confidence level. Standard cosmological parameters are adopted, as follows: $\langle H_0\rangle = 70\,{\rm km\,s^{-1}\,Mpc^{-1}}$, $\langle q_0\rangle = 0.0$, and $\langle \Omega_\Lambda\rangle = 73$.

2. Sample Selection and Data Reduction

2.1. Selection Rule

To better constrain and properly study the physical and geometrical properties of AGNs, we utilize the sample reported in Fischer et al. (2013), who measured the nuclear inclinations of 17 nearby AGNs ($z < 0.1$) in optical. In these 17 AGNs, 15 sources have high-quality NuSTAR archival data (the two sources without NuSTAR archival data are Mrk 279 and NGC 1667). All 15 sources also have XMM-Newton archival observations; for six of these 15 sources, the NuSTAR and XMM-Newton observations were taken simultaneously. We also supplement Chandra data for three sources, i.e., Mrk 34, Mrk 78, and Mrk 1066, for which the XMM-Newton spectra are not high quality. The summary of the observations is reported in Table 1.

It is worth mentioning that two sources in the Fischer et al. (2013) sample are excluded in our analysis: Circinus and NGC 1068. The Circinus AGN X-ray spectra have been shown to be contaminated by two bright off-nuclear X-ray sources: the X-ray binary CGX1 and the supernova remnant CGX2 (Bauer et al. 2001). Furthermore, Arévalo et al. (2014) showed that the contamination from CGX1 and CGX2 contributes to 18% of the nuclear flux in the iron line region and becomes comparable to the nuclear flux at energy >30 keV. The off-nuclear sources can be resolved by XMM-Newton but not by NuSTAR. Therefore, Circinus is excluded from our sample due to the fact we do not have the ability to extract the AGN broadband X-ray spectrum of Circinus without any contamination. Furthermore, NGC 1068 is also excluded from our final sample, since we find that it is difficult to fit both NuSTAR and XMM-Newton spectra properly with the standard model presented in Section 3.1. Indeed, Bauer et al. (2015) suggests a best-fit model of three reprocessed components with distinct column densities, rather than the single reprocessed component used in our analysis. Therefore, 13 sources are analyzed as our finalized sample in the rest of the work.

2.2. Data Reduction

2.2.1. NuSTAR

For NuSTAR data, the raw files are calibrated, cleaned, and screened using the NuSTAR `nupipeline` script version 0.4.6 and calibration database (CALDB) version 20181030. The sources spectra, ancillary response files (ARF), and response matrix files (RMF) are obtained using the `nuproducts` script version 0.3.0. The sources spectra are extracted from a 75″ circular region, unless otherwise indicated, corresponding to ≈80% of the encircled energy fraction (EEF) at 10 keV, centered on the source. The background spectra are extracted using a 75″ circular region near the source but avoiding contamination from it.

2.2.2. XMM-Newton

The XMM-Newton observations are taken with two MOS cameras (Turner et al. 2001) and the EPIC CCD cameras (pn; Strüder et al. 2001). The XMM-Newton data are reduced using the Science Analysis System (Jansen et al. 2001) version 17.0.0 following standard procedures. The source spectra are extracted from a circular region with radius of 15″ (corresponding to ≈70% of the EEF at 1.5 keV) or 30″ (corresponding to ≈85% of the EEF at 1.5 keV), based on which spectra have higher signal-to-noise ratios; the background spectra are extracted from a circle nearby the source with the same radius as the source spectra but avoiding contamination from sources. ARF and RMF files are produced using the tasks `arfgen` and `rmfgen`.

Table 1
Inclination Angle of the 15 Sources in Fischer et al. (2013)

Source	z	$\log(M_{BH})$[a]	i_{AGN}[b] (deg)	θ_{max}[c] (deg)	NuSTAR Date	NuSTAR[d] (ks)	XMM Date	XMM[e] (ks)	Chandra Date	Chandra[f] (ks)
Circinus	0.00145	6.23	65	41	2013 Jan 25	108	2013 Feb 3	131		
Mrk 3	0.01351	8.65	85	51	2015 Apr 8	50	2015 Apr 8	7		
Mrk 34	0.05050	7.12	65	40	2013 Sept 19	48	2005 Apr 4	31	2017 Jan 30	100
Mrk 78	0.03715	7.87	60	35	2018 Nov 19	48	2006 Mar 11	16	2017 Jan 1	50
…	…	…	…	…	…	…	…	…	2017 Jan 7	50
Mrk 573	0.01718	7.28	60	53	2018 Jan 6	64	2004 Jan 15	33		
Mrk 1066	0.01202	7.01	80	25	2014 Dec 6	60	2005 Feb 20	33	2003 July 14	20
NGC 1068	0.00379	7.20	85	40	2015 Feb 5	108	2015 Feb 3	89		
NGC 3227	0.00386	7.56	15	55	2016 Dec 1	84	2016 Dec 1	176		
NGC 3783	0.00973	6.94	15	55	2016 Dec 11	52	2016 Dec 11	126		
NGC 4051	0.00234	6.24	12	25	2013 Oct 9	100	2009 June 10	71		
NGC 4151	0.00332	7.66	45	33	2012 Nov 14	124	2012 Nov 14	16		
NGC 4507	0.01180	8.26	47	50	2015 June 10	68	2010 Aug 3	51		
NGC 5506	0.00618	7.94	80	40	2014 Apr 1	114	2015 July 8	322		
NGC 5643	0.00400	6.44	65	55	2014 May 24	42	2009 July 25	92		
…	…	…	…	…	2014 June 30	40	…	…		
NGC 7674	0.02892	7.56	60	40	2014 Sept 30	104	2004 June 2	22		

Notes.
[a] Logarithm of the mass of the black hole at the center of the AGN in solar mass. Circinus: Beifiori et al. (2012); Mrk 3, Mrk 78, Mrk 573, Mrk 1066: Nelson & Whittle (1995); Mrk 34: Gandhi et al. (2014); NGC 1068: Merritt & Ferrarese (2001); NGC 3227: Onken et al. (2003); NGC 3783: Onken & Peterson (2002); NGC 4051: Denney et al. (2009), NGC 4151: Onken et al. (2007); NGC 4507: Nicastro et al. (2003); NGC 5506: Nikołajuk et al. (2009); NGC 5643: Goulding et al. (2010); NGC 7674: Woo & Urry (2002).
[b] AGN inclination angle reported in Fischer et al. (2013): 0° corresponds to a "face-on" orientation. The typical error is 5°.
[c] The opening angle between the bicone axis and the outer edge of the narrow line region, assuming a typical error of 5°.
[d] Total effective exposure time after data cleaning of NuSTAR FPMA and FPMB.
[e] Total effective exposure time after data cleaning of XMM-Newton MOS1, MOS2, and pn.
[f] Effective exposure time after data cleaning for ACIS-S of Chandra.

2.2.3. Chandra

Archived Chandra ACIS-S observations are used for three sources (Mrk 34, Mrk 78, and Mrk 1066), which have low-quality XMM-Newton data because of their short exposure time and low observing luminosity in soft X-ray band. We reduced the Chandra data using Chandra's data analysis system, CIAO software package (Fruscione et al. 2006) version 4.11 and Chandra CALDB version 4.8.2. The level = 1 data are reprocessed as suggested to apply updated calibrations as suggested using the CIAO `chandra_repro` script. The source spectrum is extracted from a circular region centered at the source with a radius of 5″; the background spectrum is extracted from a circular region near the source with a radius of 10″. The CIAO `specextract` tool is used to extract both source and background spectra as well as ARF and RMF files following standard procedures.

The NuSTAR, XMM-Newton, and Chandra spectra are rebinned with a minimum of 20 counts per bin using the HEAsoft task `grppha`.

3. Spectral Analysis and Results

The spectra are fitted using the `XSPEC` software (Arnaud 1996) version 12.10.0 c. The photoelectric cross section for the absorption component is from Verner et al. (1996), the element abundance is from Anders & Grevesse (1989), and the metal abundance is fixed to solar. The Galactic absorption column density is obtained using the `nh` task (Kalberla et al. 2005) in `HEAsoft` for each source. The redshift of each source is adopted from NED.[6] In this work, the spectra are analyzed using the self-consistent `borus02` model (Baloković et al. 2018), which is suitable to characterize AGNs with high-quality broadband X-ray spectra.

3.1. Spectral Modeling

The recently published Monte Carlo radiative transfer code `BORUS` (Baloković 2017) has already been widely used to model the reprocessed component of AGN spectra (e.g., Boorman et al. 2018; Kammoun et al. 2019; la Caria et al. 2019; Li et al. 2019; Marchesi et al. 2019; Masini et al. 2019); see also the `borus02` website[7] for more details. The complete model used in fitting the spectra is composed of four parts:

1. An absorbed intrinsic continuum, described by a cutoff power law, denoted by `cutoffpl` in `XSPEC`, multiplied by a obscuring component, considering both the photo-electric absorption (`zphabs`) and the Compton scattering (`cabs`) effects.
2. A reprocessed component produced by the obscuring material near the center of the AGN, including the scattered component and fluorescent lines, characterized by `borus02`.
3. A second, leaked unabsorbed intrinsic continuum, modeling the fractional AGN emission that is deflected rather than absorbed by the obscuring material.
4. A thermal component, namely, `mekal` (Mewe et al. 1985), modeling the soft excess observed below 1 keV, potentially describing the emission caused by the

[6] https://ned.ipac.caltech.edu

[7] http://www.astro.caltech.edu/~mislavb/download/

processes other than AGNs, such as star formation and/or diffuse gas emission.

The reprocessed component, `borus02`[8] assumes a sphere with conical cutouts at both poles (Baloković et al. 2018), approximating a torus with an opening angle that can vary in the range of $\theta_{\rm Tor} = [0–84]^\circ$, corresponding to a torus covering factor, $c_{\rm f} = \cos(\theta_{\rm Tor}) = [1–0.1]$. Another parameter in the reprocessed component is the inclination angle, which is the angle between the axis of the AGN and the observer line of sight, $\theta_{\rm inc} = [18–87]^\circ$, where $\theta_{\rm obs} = 0^\circ$ is when the AGN is observed "face-on" and $\theta_{\rm obs} = 87^\circ$ is when the AGN is observed "edge-on." Another parameter, the relative iron abundance of the reprocessed component, $A_{\rm Fe}$, is fixed to 1 (i.e., the iron abundance in solar, $A_{\rm Fe,\odot}$), unless a much better result is obtained, leaving the parameter free to vary. We plot the spectra of the `borus02` (Baloković et al. 2018) model prediction when varying different parameters in Appendix A to illustrate how the spectra of the reprocessed component vary with different parameters, i.e., $\theta_{\rm obs}$, $\theta_{\rm Tor}$, $\theta_{\rm Tor}$, and $A_{\rm Fe}$. Evidence in Infrared and X-ray observations have shown that the torus is clumpy rather than having a uniform density (e.g., Krolik & Begelman 1988; Risaliti et al. 2002; Nenkova et al. 2008; Almeida et al. 2009; Markowitz et al. 2014). Therefore, the column density of the obscuring torus in the reprocessed component is decoupled from the one in the absorbed intrinsic continuum in our modeling to approximate the clumpy nature of the obscuring torus. In this scenario, the column density of the reprocessed component is an average property of the clumpy torus while the column density of the absorbed intrinsic continuum represents a line-of-sight quantity.

In the process of modeling the spectra, photon index, Γ, cutoff energy, $E_{\rm cut}$, and normalization, *norm*, of the intrinsic continuum, the reprocessed component and the fractional unabsorbed continuum are tied together, assuming that the three component have the same origin. The cutoff energy is fixed at $E_{\rm cut} = 500$ keV, unless a much better result is obtained, leaving the parameter free to vary. The fractional unabsorbed continuum is usually less than 5%–10% of the intrinsic continuum (see, e.g., Noguchi et al. 2010; Marchesi et al. 2018). We denote this fraction as f_s, and we model it with a constant ($\texttt{constant}_2$). Finally, the temperature and the relative metal abundance in `mekal` are both left free to vary. Lines are added if strong emission lines are found in the spectra using the `zgauss` model in `XSPEC`.

The `borus02` model is used in the following `XSPEC` configuration:

$$Model = constant_1 * phabs * (borus02 + zphabs * cabs * cutoffpl + constant_2 * cutoffpl + mekal)$$

where $\texttt{constant}_1$ is the cross-calibration between NuSTAR and XMM-Newton (separate cross-calibration constants are applied if Chandra data are used); `phabs` models the Galactic absorption.

3.2. Results

We fit the spectra twice at first: leaving the inclination angle free to vary when fitting the spectra and fixing the inclination angle at the values reported in Fischer et al. (2013). The best-fit results are reported in Tables 2 and 3. Furthermore, to extend our analysis on the role of inclination angle in the spectral analysis, we also fit the spectra by fixing the inclination at some specific angles, i.e., $\theta_{\rm inc} = 60^\circ$ or $\cos(\theta_{\rm inc}) = 0.5$ (i.e., the opening angle of the torus in MYTorus model Murphy & Yaqoob 2009), and fixing inclination at $\theta_{\rm inc} = 87^\circ$ (the maximum angle in `borus02` model) representing an "edge-on" scenario, which is commonly used when analyzing heavily obscured AGN spectra (see, e.g., Brightman & Nandra 2011; Koss et al. 2015; Ricci et al. 2016; Marchesi et al. 2018; Zappacosta et al. 2018); although, not all of the sources in our sample are heavily obscured. The best-fit results of the two scenarios are also reported in Tables 2 and 3. The details of the fitting procedure of each source and best-fit results of the 13 sources fitted when the inclination angles are left free to vary are reported in Appendix C. The unfolded spectra and the model predictions of each source when fitted, leaving the inclination angle free to vary, are plotted in Appendix C as well.

Six out of 13 sources in our sample have been observed to display strong variability between their soft X-ray observations and NuSTAR observations. The observed variability is commonly explained by either the variation of the accretion rate of the SMBH or the variation in the so-called corona when the fluctuation of intrinsic emission of the AGN is observed, i.e., the shape of the spectrum does not change while the normalization of the intrinsic power law varies (Nandra 2001), or there is change in the absorption column density along the line of sight when the shape of the spectra varies (see, e.g., Risaliti et al. 2002; Bianchi et al. 2012), or both. To properly characterize the spectra of these sources, we fit them three times: (1) disentangling the normalization of the intrinsic cutoff power law, `norm`, of the soft X-ray observatories' observations and the NuSTAR observations, modeling the flux variability caused by the intrinsic emission variation; (2) disentangling the line-of-sight column densities of the soft X-ray observations, $N_{\rm H,los,soft}$ and NuSTAR observations, $N_{\rm H,los,NuS}$, modeling the flux variability results from the line-of-sight column density variability; (3) disentangling both the norm and $N_{\rm H,los}$ between the soft X-ray observations and the NuSTAR observations, assuming the flux variability is caused by both the intrinsic emission variation and line-of-sight column density variability. Here, we treat the reprocessed emission as an invariable component during the two observations, assuming a stable structure and constant global properties of the obscuring torus.

The decoupling line-of-sight column density and the torus average column density applied to fit the spectra in this work are commonly used to approximate the nonuniform (clumpy) torus. To interpret the obtained results, we separate the sources into three categories.

1. Obscured AGNs with $\log(N_{\rm H,l.o.s}) \geqslant 22$ where the line of sight does not intercept the torus ($\cos(\theta_{\rm inc}) > c_{\rm f,tor}$), i.e., Mrk 34, NGC 3783, and NGC 5643. The interpretation of this result is that an obscured clump is above the torus along our line of sight. However, we cannot exclude the possibility that the inclination angle smaller than the half-opening angle of the torus ($\cos(\theta_{\rm inc}) > c_{\rm f,tor}$) may correspond to a clumpy torus seen edge-on (see Figure 3 and Section 2.3 in Baloković et al. 2018) and (Figure 6.1 in Baloković 2017).

[8] The energy coverage of the `borus02` model is 1 keV $< E <$ 1000 keV. The model cutoff at 1 keV does not affect the fit of the sources in our sample since their spectra in soft energy band ($E < 3$ keV) are dominated by the leaked component.

Table 2
Best-fit Results of the 13 Sources

Model	χ^2/d.o.f.	Γ	$N_{\rm H,l.o.s}$[a]	$N_{\rm H,tor}$[b]	$\cos(\theta_{\rm inc})$[c]	$c_{\rm f,tor}$[d]	Norm[e]	f_s[f]	F_{2-10}[g]	$L_{\rm int}$[h]
					Mrk 3					
Free	1056/1073	$1.48^{+0.11}_{-u}$	$23.94^{+0.06}_{-0.04}$	$23.30^{+0.24}_{-0.15}$	$0.47^{+0.16}_{-0.07}$	$0.50^{+0.06}_{-0.22}$	$1.42^{+0.54}_{-0.22}$	$0.98^{+0.46}_{-0.89}$	8^{+1}_{-4}	31
[O III]	1061/1074	$1.40^{+0.05}_{-u}$	$23.91^{+0.01}_{-0.05}$	$23.04^{+0.24}_{-0.26}$	0.09[f]	$0.62^{+0.28}_{-0.05}$	$1.12^{+0.01}_{-0.11}$	$1.36^{+0.55}_{-0.14}$	8^{+2}_{-4}	28
60°	1057/1074	$1.46^{+0.18}_{-u}$	$23.95^{+0.06}_{-0.05}$	$23.32^{+0.44}_{-0.24}$	0.50[f]	$0.50^{+0.06}_{-0.17}$	$1.35^{+0.82}_{-0.17}$	$0.81^{+0.36}_{-0.50}$	8^{+1}_{-5}	31
87°	1061/1074	$1.40^{+0.12}_{-u}$	$23.90^{+0.02}_{-0.04}$	$23.07^{+0.19}_{-0.31}$	0.05[f]	$0.60^{+0.29}_{-0.04}$	$1.12^{+0.01}_{-0.11}$	$1.41^{+0.44}_{-0.14}$	8^{+3}_{-3}	28
					Mrk 34					
Free	74/82	$1.45^{+0.67}_{-u}$	$24.74^{+u}_{-0.46}$	$25.04^{+u}_{-0.73}$	0.42^{+u}_{-u}	$0.40^{+0.44}_{-0.27}$	$0.06^{+0.35}_{-0.03}$	$0.85^{+2.02}_{-0.65}$	$0.2^{+18}_{-0.2}$	21
[O III]	74/83	$1.49^{+0.59}_{-u}$	$24.73^{+u}_{-0.34}$	$24.98^{+u}_{-0.64}$	0.42[f]	$0.41^{+0.06}_{-0.31}$	$0.07^{+0.56}_{-0.02}$	$0.74^{+0.53}_{-0.53}$	$0.2^{+3.7}_{-0.2}$	24
60°	74/83	$1.46^{+0.55}_{-u}$	$24.67^{+u}_{-0.36}$	$25.00^{+u}_{-0.71}$	0.50[f]	$0.43^{+0.09}_{-u}$	$0.05^{+0.47}_{-0.10}$	$1.12^{+0.65}_{-0.82}$	$0.2^{+2.2}_{-0.2}$	16
87°	76/83	$1.41^{+0.33}_{-u}$	$24.59^{+0.08}_{-0.04}$	$23.66^{+0.17}_{-0.09}$	0.05[f]	$0.10^{+0.13}_{-u}$	$0.25^{+0.07}_{-0.02}$	$0.29^{+0.06}_{-0.05}$	$0.2^{+0.5}_{-0.2}$	96
					Mrk 78					
Free	276/271	$1.40^{+0.21}_{-u}$	$23.91^{+0.13}_{-0.02}$	$24.21^{+0.18}_{-0.33}$	$0.43^{+0.45}_{-0.18}$	$0.45^{+u}_{-0.23}$	$0.06^{+0.00}_{-0.03}$	$1.80^{+2.00}_{-0.20}$	$0.5^{+0.3}_{-0.5}$	12
[O III]	276/272	$1.40^{+0.22}_{-u}$	$23.89^{+0.07}_{-0.07}$	$24.15^{+0.15}_{-0.25}$	0.50[f]	$0.54^{+u}_{-0.12}$	$0.05^{+0.00}_{-0.01}$	$2.19^{+1.56}_{-0.23}$	$0.5^{+0.2}_{-0.5}$	10
60°	276/272	$1.40^{+0.22}_{-u}$	$23.89^{+0.07}_{-0.07}$	$24.15^{+0.15}_{-0.25}$	0.50[f]	$0.54^{+u}_{-0.12}$	$0.05^{+0.00}_{-0.01}$	$2.19^{+1.56}_{-0.23}$	$0.5^{+0.2}_{-0.5}$	10
87°	278/272	$1.40^{+0.16}_{-u}$	$23.82^{+0.06}_{-0.02}$	$23.95^{+0.07}_{-0.06}$	0.05[f]	$0.99^{+u}_{-0.34}$	$0.04^{+0.00}_{-0.01}$	$3.32^{+0.90}_{-0.29}$	$0.5^{+0.1}_{-0.3}$	8.0
					Mrk 573					
Free	152/194	$2.35^{+u}_{-0.65}$	$24.52^{+u}_{-0.30}$	$24.91^{+u}_{-0.68}$	0.60^{+u}_{-u}	$0.61^{+0.37}_{-u}$	$0.56^{+2.25}_{-0.51}$	$0.17^{+1.91}_{-0.19}$	$0.3^{+10}_{-0.3}$	5.7
[O III]	152/195	$2.36^{+u}_{-0.62}$	$24.63^{+u}_{-0.32}$	$25.00^{+u}_{-0.73}$	0.50[f]	$0.54^{+0.04}_{-u}$	$0.96^{+2.58}_{-0.87}$	$0.10^{+1.13}_{-0.10}$	$0.3^{+12}_{-0.3}$	9.7
60°	152/195	$2.36^{+u}_{-0.62}$	$24.63^{+u}_{-0.32}$	$25.00^{+u}_{-0.73}$	0.50[f]	$0.54^{+0.04}_{-u}$	$0.96^{+2.58}_{-0.87}$	$0.10^{+1.13}_{-0.10}$	$0.3^{+12}_{-0.3}$	9.7
87°	152/195	$2.60^{+u}_{-0.02}$	$24.94^{+u}_{-0.05}$	$24.99^{+0.04}_{-0.02}$	0.05[f]	$0.12^{+0.06}_{-u}$	110^{+6}_{-8}	$0.00^{+0.01}_{-0.00}$	$0.3^{+1.1}_{-0.3}$	798
					Mrk 1066					
Free	142/147	$1.52^{+0.02}_{-u}$	$23.97^{+0.03}_{-0.05}$	$24.16^{+0.31}_{-0.10}$	0.65^{+u}_{-u}	$1.00^{+u}_{-0.36}$	$0.08^{+0.11}_{-0.01}$	$4.05^{+2.38}_{-2.36}$	$0.3^{+0.1}_{-0.3}$	1.1
[O III]	142/148	$1.53^{+0.06}_{-0.06}$	$23.98^{+0.03}_{-0.07}$	$24.17^{+0.06}_{-0.05}$	0.17[f]	$1.00^{+u}_{-0.37}$	$0.08^{+0.02}_{-0.01}$	$4.04^{+1.51}_{-0.47}$	$0.3^{+0.1}_{-0.3}$	1.1
60°	142/148	$1.54^{+0.02}_{-0.04}$	$23.98^{+0.00}_{-0.02}$	$24.17^{+0.01}_{-0.02}$	0.50[f]	$1.00^{+u}_{-0.36}$	$0.09^{+0.01}_{-0.00}$	$3.78^{+0.63}_{-0.08}$	$0.3^{+0.1}_{-0.3}$	1.2
87°	142/148	$1.53^{+0.06}_{-0.03}$	$23.97^{+0.04}_{-0.06}$	$24.17^{+0.04}_{-0.07}$	0.05[f]	$1.00^{+u}_{-0.36}$	$0.09^{+0.10}_{-0.03}$	$3.78^{+2.32}_{-0.70}$	$0.3^{+0.1}_{-0.3}$	1.2
					NGC 3227					
Free	4684/4008	$1.68^{+0.01}_{-0.01}$	$21.39^{+0.03}_{-0.01}$	$23.14^{+0.03}_{-0.02}$	$0.15^{+0.14}_{-u}$	$1.00^{+u}_{-0.07}$	$0.86^{+0.01}_{-0.01}$	0[f]	$37.7^{+0.3}_{-0.2}$	1.2
[O III]	4686/4009	$1.68^{+0.01}_{-0.01}$	$21.39^{+0.05}_{-0.04}$	$23.14^{+0.03}_{-0.04}$	0.95[f]	$1.00^{+u}_{-0.05}$	$0.86^{+0.01}_{-0.01}$	0[f]	$37.7^{+0.2}_{-0.1}$	1.2
60°	4686/4009	$1.68^{+0.01}_{-0.01}$	$21.39^{+0.05}_{-0.06}$	$23.14^{+0.03}_{-0.04}$	0.95[f]	$1.00^{+u}_{-0.13}$	$0.86^{+0.01}_{-0.01}$	0[f]	$37.7^{+0.1}_{-0.1}$	1.2
87°	4686/4009	$1.68^{+0.01}_{-0.01}$	$21.39^{+0.05}_{-0.06}$	$23.15^{+0.03}_{-0.04}$	0.05[f]	$1.00^{+u}_{-0.11}$	$0.87^{+0.01}_{-0.02}$	0[f]	$37.7^{+0.3}_{-0.3}$	1.2
					NGC 3783					
Free	3349/2929	$1.51^{+0.02}_{-0.04}$	$22.85^{+0.01}_{-0.01}$	$25.00^{+0.11}_{-0.22}$	$0.54^{+0.02}_{-0.02}$	$0.41^{+0.08}_{-0.04}$	$0.68^{+0.03}_{-0.03}$	$10.14^{+0.30}_{-0.28}$	26^{+1}_{-1}	6.9
[O III]	3367/2930	$1.49^{+0.04}_{-0.02}$	$22.84^{+0.02}_{-0.01}$	$25.11^{+u}_{-0.23}$	0.95[f]	$0.26^{+0.01}_{-0.01}$	$0.66^{+0.05}_{-0.03}$	$10.55^{+0.39}_{-0.70}$	26^{+1}_{-2}	6.9
60°	3356/2930	$1.49^{+0.01}_{-0.05}$	$22.85^{+0.01}_{-0.01}$	$24.98^{+0.12}_{-0.27}$	0.50[f]	$0.40^{+0.01}_{-0.02}$	$0.67^{+0.02}_{-0.05}$	$10.42^{+0.11}_{-0.33}$	26^{+1}_{-2}	6.9
87°	3439/2930	$1.55^{+0.01}_{-0.01}$	$22.82^{+0.01}_{-0.01}$	$23.58^{+0.06}_{-0.08}$	0.05[f]	$1.00^{+u}_{-0.03}$	$0.66^{+0.01}_{-0.04}$	$10.47^{+0.69}_{-0.18}$	27^{+0}_{-1}	6.8

Notes.
[a] Logarithm of line-of-sight column density in $\rm cm^{-2}$; for sources for which variability has been observed between the NuSTAR and XMM-Newton, we report here the line-of-sight column density of the XMM-Newton observation.
[b] Logarithm of average torus column density in $\rm cm^{-2}$.
[c] Inclination angle, i.e., the angle between the axis of the torus and the edge of the torus.
[d] Effective covering factor of the torus.
[e] Normalization of the main cutoff power-law component at 1 keV in 10^{-2} photons $\rm keV^{-1}$ $\rm cm^{-2}$ $\rm s^{-1}$ of XMM-Newton observations.
[f] Fraction of scattering component in 10^{-2}.
[g] Flux between 2 and 10 keV in 10^{-12} erg $\rm cm^{-2}$ $\rm s^{-1}$ of XMM-Newton observation.
[h] Intrinsic luminosity between 2 and 10 keV in 10^{42} erg $\rm s^{-1}$ of XMM-Newton observation.

Table 3
Best-fit Results of the 13 Sources

Model	χ^2/d.o.f.	Γ	$N_{\rm H,l.o.s}$[a]	$N_{\rm H,tor}$[b]	$\cos(\theta_{\rm inc})$[c]	$c_{\rm f,tor}$[d]	Norm[e]	f_s[f]	F_{2-10}[g]	$L_{\rm int}$[h]
					NGC 4051					
Free	2686/2390	$1.72^{+0.01}_{-0.01}$	$22.53^{+0.01}_{-0.01}$	$24.45^{+0.07}_{-0.09}$	$0.95^{+u}_{-0.01}$	$0.95^{+0.01}_{-0.01}$	$0.45^{+0.01}_{-0.01}$	0^{f}	14^{+1}_{-1}	0.2
[O III]	2686/2391	$1.72^{+0.01}_{-0.01}$	$22.53^{+0.01}_{-0.01}$	$24.45^{+0.07}_{-0.06}$	0.95^{f}	$0.95^{+0.01}_{-0.01}$	$0.45^{+0.01}_{-0.01}$	0^{f}	14^{+1}_{-1}	0.2
60°	2739/2391	$1.70^{+0.03}_{-0.05}$	$22.53^{+0.03}_{-0.02}$	$24.16^{+0.03}_{-0.04}$	0.50^{f}	$1.00^{+u}_{-0.04}$	$0.45^{+0.01}_{-0.02}$	0^{f}	14^{+0}_{-2}	0.2
87°	2738/2391	$1.70^{+0.03}_{-0.05}$	$22.53^{+0.03}_{-0.01}$	$24.16^{+0.03}_{-0.05}$	0.05^{f}	$1.00^{+u}_{-0.02}$	$0.45^{+0.01}_{-0.02}$	0^{f}	14^{+0}_{-2}	0.2
					NGC 4151					
Free	5200/4664	$1.67^{+0.02}_{-0.04}$	$23.00^{+0.01}_{-0.01}$	$23.94^{+0.02}_{-0.02}$	$0.05^{+0.03}_{-u}$	$0.80^{+0.04}_{-0.07}$	$3.64^{+0.16}_{-0.23}$	$2.75^{+0.20}_{-0.13}$	88^{+1}_{-1}	3.6
[O III]	5208/4665	$1.74^{+0.02}_{-0.01}$	$23.01^{+0.01}_{-0.00}$	$24.01^{+0.04}_{-0.03}$	0.71^{f}	$0.88^{+u}_{-0.06}$	$4.09^{+0.19}_{-0.12}$	$2.49^{+0.11}_{-0.14}$	88^{+1}_{-1}	3.7
60°	5201/4665	$1.69^{+0.03}_{-0.04}$	$23.00^{+0.02}_{-0.01}$	$23.98^{+0.02}_{-0.02}$	0.50^{f}	$0.78^{+0.08}_{-0.09}$	$3.75^{+0.22}_{-0.27}$	$2.68^{+0.23}_{-0.16}$	88^{+1}_{-1}	3.6
87°	5200/4665	$1.67^{+0.02}_{-0.04}$	$23.00^{+0.01}_{-0.01}$	$23.94^{+0.04}_{-0.03}$	0.05^{f}	$0.80^{+0.04}_{-0.06}$	$3.64^{+0.16}_{-0.24}$	$2.75^{+0.20}_{-0.13}$	88^{+1}_{-1}	3.6
					NGC 4507					
Free	1601/1614	$1.71^{+0.05}_{-0.03}$	$23.98^{+0.03}_{-0.05}$	$23.40^{+0.09}_{-0.09}$	$0.43^{+0.10}_{-0.13}$	$0.55^{+0.09}_{-0.06}$	$2.03^{+0.40}_{-0.46}$	$0.27^{+0.18}_{-0.19}$	$7.1^{+0.3}_{-0.3}$	25
[O III]	1603/1615	$1.85^{+0.04}_{-0.02}$	$23.87^{+0.02}_{-0.02}$	$25.50^{+u}_{-0.19}$	0.68^{f}	$0.40^{+0.06}_{-0.06}$	$1.67^{+0.24}_{-0.10}$	$0.18^{+0.15}_{-0.02}$	$7.1^{+0.2}_{-0.3}$	17
60°	1603/1615	$1.68^{+0.02}_{-0.05}$	$23.98^{+0.02}_{-0.06}$	$23.44^{+0.04}_{-0.11}$	0.50^{f}	$0.59^{+0.07}_{-0.04}$	$1.81^{+0.14}_{-0.34}$	$0.23^{+0.17}_{-0.18}$	$7.1^{+0.2}_{-0.3}$	23
87°	1607/1615	$1.69^{+0.06}_{-0.04}$	$23.97^{+0.05}_{-0.03}$	$23.34^{+0.06}_{-0.05}$	0.05^{f}	$0.63^{+0.08}_{-0.05}$	$1.89^{+0.52}_{-0.29}$	$0.43^{+0.10}_{-0.09}$	$7.1^{+0.1}_{-0.3}$	24
					NGC 5506					
Free	5378/4543	$1.72^{+0.01}_{-0.01}$	$22.50^{+0.01}_{-0.00}$	$23.91^{+0.02}_{-0.02}$	$0.55^{+0.09}_{-0.25}$	$1.00^{+u}_{-0.02}$	$1.90^{+0.03}_{-0.01}$	$1.33^{+0.04}_{-0.04}$	61^{+4}_{-0}	4.9
[O III]	5381/4544	$1.72^{+0.02}_{-0.01}$	$22.50^{+0.01}_{-0.00}$	$23.91^{+0.01}_{-0.01}$	0.17^{f}	$1.00^{+u}_{-0.02}$	$1.90^{+0.04}_{-0.03}$	$1.33^{+0.04}_{-0.05}$	61^{+4}_{-1}	4.9
60°	5379/4544	$1.72^{+0.01}_{-0.01}$	$22.50^{+0.01}_{-0.00}$	$23.91^{+0.02}_{-0.02}$	0.50^{f}	$1.00^{+u}_{-0.02}$	$1.90^{+0.03}_{-0.02}$	$1.33^{+0.04}_{-0.05}$	61^{+4}_{-0}	4.9
87°	5380/4544	$1.72^{+0.02}_{-0.01}$	$22.50^{+0.01}_{-0.00}$	$23.91^{+0.01}_{-0.01}$	0.05^{f}	$1.00^{+u}_{-0.02}$	$1.90^{+0.04}_{-0.03}$	$1.33^{+0.04}_{-0.05}$	61^{+5}_{-1}	4.9
					NGC 5643					
Free	198/170	$1.77^{+0.27}_{-0.37}$	$24.65^{+u}_{-0.32}$	$24.15^{+0.22}_{-0.35}$	$0.51^{+u}_{-0.24}$	$0.50^{+0.38}_{-0.23}$	$0.41^{+1.23}_{-0.27}$	$0.10^{+0.39}_{-0.10}$	$0.8^{+15}_{-0.6}$	0.5
[O III]	199/171	$1.77^{+0.32}_{-0.34}$	$24.65^{+0.23}_{-0.25}$	$24.13^{+0.23}_{-0.28}$	0.42^{f}	$0.42^{+0.04}_{-0.13}$	$0.51^{+0.63}_{-0.28}$	$0.08^{+0.28}_{-0.08}$	$0.8^{+19}_{-0.3}$	0.6
60°	198/171	$1.80^{+0.27}_{-0.32}$	$24.65^{+u}_{-0.28}$	$24.15^{+0.24}_{-0.31}$	0.50^{f}	$0.49^{+0.04}_{-0.12}$	$0.47^{+0.54}_{-0.25}$	$0.10^{+0.31}_{-0.10}$	$0.8^{+17}_{-0.5}$	0.6
87°	220/171	$1.40^{+0.12}_{-u}$	$24.35^{+0.06}_{-0.05}$	$23.44^{+0.04}_{-0.08}$	0.05^{f}	$0.43^{+0.03}_{-0.07}$	$0.12^{+0.01}_{-0.01}$	$1.59^{+0.21}_{-0.21}$	$0.8^{+0.4}_{-0.6}$	0.3
					NGC 7674					
Free	240/251	$2.21^{+0.12}_{-0.18}$	$24.15^{+0.08}_{-0.05}$	$23.65^{+0.14}_{-0.05}$	$0.25^{+0.52}_{-0.04}$	$0.10^{+0.15}_{-u}$	$1.49^{+2.87}_{-0.06}$	0^{f}	$0.6^{+0.6}_{-0.6}$	54
[O III]	241/252	$2.20^{+0.17}_{-0.19}$	$24.13^{+0.06}_{-0.06}$	$23.73^{+0.11}_{-0.05}$	0.50^{f}	$0.10^{+0.07}_{-u}$	$1.26^{+0.36}_{-0.06}$	0^{f}	$0.7^{+0.2}_{-0.7}$	46
60°	241/252	$2.20^{+0.17}_{-0.19}$	$24.13^{+0.06}_{-0.06}$	$23.73^{+0.11}_{-0.05}$	0.50^{f}	$0.10^{+0.07}_{-u}$	$1.26^{+0.36}_{-0.06}$	0^{f}	$0.7^{+0.2}_{-0.7}$	46
87°	245/251	$2.00^{+0.40}_{-0.31}$	$24.10^{+0.15}_{-0.17}$	$23.27^{+0.13}_{-0.18}$	0.05^{f}	$0.30^{+0.39}_{-u}$	$0.66^{+1.65}_{-0.49}$	$0.60^{+1.47}_{-0.04}$	$0.7^{+0.1}_{-0.7}$	32

Notes.
[a] Logarithm of line-of-sight column density in $\rm cm^{-2}$; for sources for which variability has been observed between the NuSTAR and XMM-Newton, we report here the line-of-sight column density of the XMM-Newton observation.
[b] Logarithm of average torus column density in $\rm cm^{-2}$.
[c] Inclination angle, i.e., the angle between the axis of the torus and the edge of the torus.
[d] Effective covering factor of the torus.
[e] Normalization of the main cutoff power-law component at 1 keV in 10^{-2} photons $\rm keV^{-1}\ cm^{-2}\ s^{-1}$ of XMM-Newton observations.
[f] Fraction of scattering component in 10^{-2}.
[g] Flux between 2 and 10 keV in 10^{-12} erg $\rm cm^{-2}\ s^{-1}$ of XMM-Newton observation.
[h] Intrinsic luminosity between 2 and 10 keV in 10^{42} erg $\rm s^{-1}$ of XMM-Newton observation.

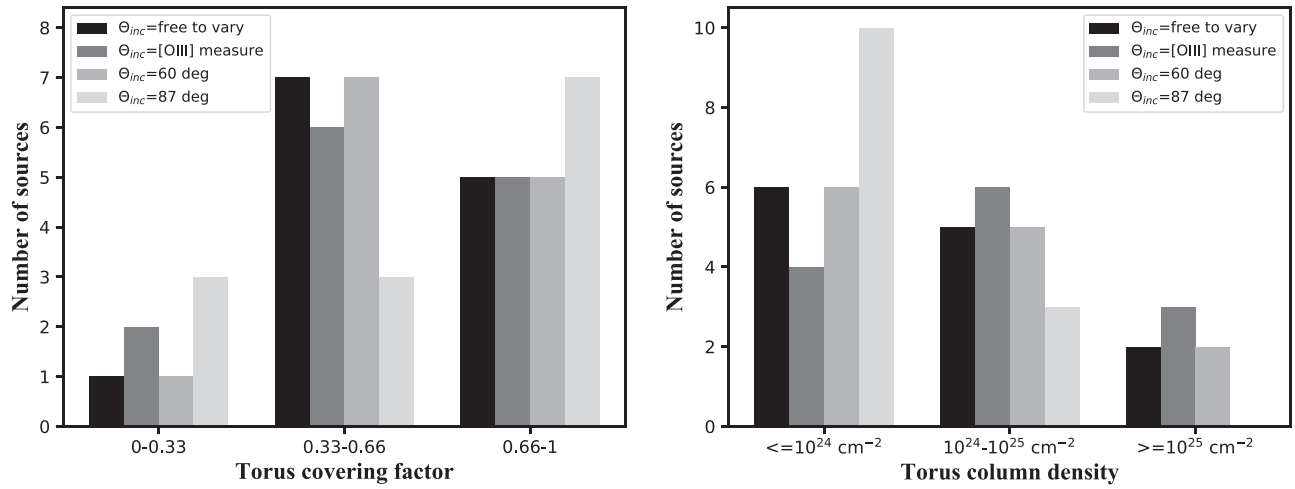

Figure 1. The number of sources with specific best-fit torus covering factor (left panel) and torus column density (right panel) are shown. From left to right in each panel, these are shown when $\theta_{\rm inc}$ is left free to vary (black histogram), when $\theta_{\rm inc}$ is fixed at [O III] measured values (dark gray histogram), when $\theta_{\rm inc}$ is fixed at $\theta_{\rm inc} = 60°$ (light gray histogram), and $\theta_{\rm inc} = 87°$ (silver histogram).

2. Unobscured AGN $\log(N_{\rm H,l.o.s}) < 22$ where the line of sight intercepts the torus ($\cos(\theta_{\rm inc}) \leqslant c_{\rm f,tor}$), i.e., NGC 3227. This result may suggest that the source is observed through an underdense region of a clumpy obscured torus.
3. Obscured AGNs with their line of sight intercepting the torus, but the line-of-sight column density is significantly different from the torus average column density ($|\Delta \log(N_{\rm H})| \gtrsim 1$), e.g., NGC 3227, NGC 4051, NGC 4151, and NGC 5506. This result shows that we are currently looking through either an overdense or underdense region in their nonuniform tori, and this could be changing with time (see, e.g., Risaliti et al. 2005).

4. Discussion

Thanks to the `borus02` model and the [O III] measured inclination, we are able to properly study the role of inclination angle in analyzing the AGN spectra: the best-fit results of 13 sources when fitted with different scenarios of applying the inclination angle are reported in Section 3. In the rest of the work, we discuss how varying the inclination angle affects the measurement of the other spectral parameters (Sections 4.1–4.3), discuss the correlations between the covering factor of the obscuring torus and other AGN properties (Section 4.4), and study the geometrical properties of the AGNs in both X-ray and optical (Section 4.5).

4.1. Fixing the Torus Inclination Angle at $\theta_{inc,[O\ III]}$

We compare the best-fit results of different spectral parameters (i.e., χ^2/d.o.f., Γ, $N_{\rm H,l.o.s}$, $N_{\rm H,tor}$, $c_{\rm f,tor}$, and $\theta_{\rm inc}$) computed either leaving the inclination angle free to vary or using the [O III] measured values, $\theta_{\rm inc,[O\ III]}$, reported in Fischer et al. (2013). The best-fit results obtained in two scenarios are reported in Tables 2 and 3. We compare the best-fit $c_{\rm f,tor}$ and $N_{\rm H,tor}$ computed in two methods in Figure 2. The above comparison is also plotted as a histogram in Figure 1 for better readability.

1. The inclination angles of three sources in our sample (Mrk 34, Mrk 573, and Mrk 1066) are fully unconstrained when inclination angle is left free to vary in fitting the spectra due to the poor quality (d.o.f $\leqslant$ 200) of the data.

   The best-fit inclination angles measured in X-ray do not always match the inclination angles measured in optical using [O III], e.g., we found six sources for which the differences between the two inclination angles is $\Delta\theta_{\rm inc} > 20°$.
2. In spite of the large $\Delta\theta_{\rm inc}$ found in some sources, the best-fit results of the other key parameters, e.g., $N_{\rm H,l.o.s}$, $N_{\rm H,tor}$, and $c_{\rm f,tor}$ are in good agreement with each other within the uncertainties.
3. The goodness of the spectral fits shows no improvement or only a marginal improvement when inclination angle is left free to vary in fitting the spectra. The source with the most improved fit statistics in our sample is NGC 3783, which improves from χ^2/d.o.f $= 3367/2930$ when fixing the inclination angle at the [O III] measured inclination to χ^2/d.o.f $= 3349/2929$ when leaving the inclination free to vary.
4. A minor improvement on constraining the spectral parameters is found when fixing the $\theta_{\rm inc}$ at [O III] measured value. The average uncertainties on each parameter are reported in Table 4.

Table 4
Average Uncertainties of Different Parameters Assuming Different Torus Inclination Angles

Parameter	Free to Vary	[O III]	60°	87°
Γ	10%	9%	10%	6%
$N_{\rm H,l.o.s}$	19%	18%	18%	10%
$N_{\rm H,tor}$	38%	36%	37%	17%
$c_{\rm f,tor}$[a]	0.17	0.11	0.11	0.10
χ^2_ν	1.04	1.04	1.04	1.05

Note.
[a] Absolute average uncertainty.

The above results suggest that: (1) the inclination angle measured in the optical band using [O III] can be used in the X-ray spectral analysis of AGNs, since it provides similar

best-fit results to those obtained when the inclination angle is left free to vary when fitting the spectra considering uncertainties; (2) in some sources, significant different inclination angles measured in the optical compared to those derived from the X-ray spectra are found, but the other fitted parameters, as well as the best-fit statistic, are only marginally affected by this variation, suggesting that we do not have enough power to constrain the inclination angle of these sources even with high-quality broadband X-ray data.

4.2. Fixing the Torus Inclination Angle at $\theta_{inc} = 60°$

Following the method in Section 4.1, we compare the best-fit results obtained when leaving the inclination angle free to vary with the best-fit results computed when fixing the inclination at some specific angles, e.g., $\theta_{\rm inc} = 60°$. The best-fit results when the sources are fitted with $\theta_{\rm inc} = 60°$ are reported in Tables 2 and 3. The comparison of $c_{\rm f,tor}$ and $N_{\rm H,tor}$ between the two scenarios is plotted in Figure 2. The above comparison is also plotted as a histogram in Figure 1 for better readability.

We find that the differences of the best-fit results of different parameters between when $\theta_{\rm inc} = 60°$ and when leaving $\theta_{\rm inc}$ free to vary are marginal, e.g., the average differences are ∼1% for Γ, ∼2% for $N_{\rm H,l.o.s}$, ∼5% for $N_{\rm H,tor}$, and 2% for $c_{\rm f,tor}$. We measure a similar average goodness of fitting in the two scenarios as reported in Table 4. Only marginal improvements are found in the fits of most sources when the inclination angle is left free to vary in fitting the spectra versus when the inclination angle is fixed at $\theta_{\rm inc} = 60°$, except for NGC 4051, whose fit improves from $\chi^2/{\rm d.o.f} = 2739/2391$ to $\chi^2/{\rm d.o.f} = 2686/2390$ after leaving the inclination angle free to vary. Fixing the inclination angle at $\theta_{\rm inc} = 60°$ provides similar constraints on fitting, which are consistent with those obtained when fixing $\theta_{\rm inc}$ at [O III] measured values.

Although, according to our spectral fits, fixing the inclination angle at $\theta_{\rm inc} = 60°$ provides a similar goodness of fit and similar other key properties to those when $\theta_{\rm inc}$ is left free to vary, this result may be biased by the sample that we have selected, since 9 out of 13 sources in our sample have a $\theta_{\rm inc} \sim 60°$. Indeed, we find that fixing the inclination angle at $\theta_{\rm inc} = 60°$ does not reproduce the $N_{\rm H,tor}$ or other key parameters measured when $\theta_{\rm inc}$ is left free to vary in some heavily obscured sources out of our sample, e.g., we reanalyze the spectra of a Compton thick (CT-) AGN, NGC 1358, and the best-fit $N_{\rm H,tor}$ and $c_{\rm f,tor}$ obtained when fixing the inclination angle at $\theta_{\rm inc} = 60°$ is about five times lager than those obtained when the inclination is left free to vary as reported in Zhao et al. (2019b), who measured a best-fit inclination angle of $\theta_{\rm inc,NGC\ 1358} \approx 87°$.

4.3. Fixing the Torus Inclination Angle at $\theta_{inc} = 87°$

We also fit the spectra when fixing the inclination angle at $\theta_{\rm inc} = 87°$. The differences of the best-fit results of Γ and $N_{\rm H,l.o.s}$ obtained when $\theta_{\rm inc} = 87°$ versus when leaving $\theta_{\rm inc}$ free to vary are marginal, e.g., the average differences are ∼2% for Γ and ∼9% for $N_{\rm H,l.o.s}$. However, the measurement of $N_{\rm H,tor}$ when $\theta_{\rm inc} = 87°$, especially for some sources with CT torus (i.e., $\log(N_{\rm H,tor}) \gg 24$), is considerably different (the average difference is ∼30%) from those obtained when $\theta_{\rm inc}$ is left free to vary. The discrepancy of $c_{\rm f,tor}$ between the two cases is large as well, e.g., the average difference is 22%. However, unlike in the $N_{\rm H,tor}$ case where the measurements of higher $N_{\rm H,tor}$ tend to a lower value, such a trend is not found in $c_{\rm f,tor}$. Notably, ∼30% of the sources in our sample are measured with best-fit photon indices stuck at $\Gamma \sim 1.4$, which is the lower limit of the parameter in the `borus02` model. Such a result can be explained by the fact that a flatter Γ is needed to compensate for the change of the spectral shape caused by the unrealistic measurement of $c_{\rm f,tor}$ and $N_{\rm H,tor}$. It is worth noting that fixing the inclination angle at $\theta_{\rm inc} = 87°$ leads to a significantly different best-fit torus covering factor and torus column density than when the inclination angle is left free to vary even when fitting the CT-AGNs, which are plot in red in Figure 2.

To illustrate the torus column density bias mentioned above, we take NGC 5643 as an example. The source is a CT-AGN, and the spectrum of the source is dominated by a reprocessed component. In Figure 3, we plot the spectra and different components of the model predictions of NGC 5643 for inclination angles that are fixed at $\theta_{\rm inc} = 87°$ and left free to vary. The best-fit inclination angle measured for NGC 5643 is $\theta_{\rm inc} \sim 59°$. When the inclination is left free to vary, the spectra above 2 keV are dominated by the reprocessed component, and the measured best-fit torus column density is $\log(N_{\rm H,tor,free}) \sim 24.15$. However, when the inclination angle is fixed at $\theta_{\rm inc} = 87°$, the best-fit torus column density is measured as $\log(N_{\rm H,tor,free}) \sim 23.44$. Such a result can be understood by looking at the bottom left panel of Figure 3, where we plot the `borus02` model prediction of the reprocessed component when the inclination angles are $\theta_{\rm inc} = 60°$ and $\theta_{\rm inc} = 87°$ and the torus column densities are $\log(N_{\rm H,tor,free}) = 24$ and $\log(N_{\rm H,tor,free}) = 25$. When the inclination moves from $\theta_{\rm inc} = 60°$ to $\theta_{\rm inc} = 87°$, the spectra are suppressed significantly and nonlinearly: the spectra with energy below ∼20 keV are highly affected. Therefore, the torus column density decreases to compensate for this reduction, which better describes the energy between ∼5 and ∼20 keV. The discrepancy of the spectra in other energy bands thus needs other components to make up for the reduction, e.g., the line-of-sight component contributes more to the spectra at energy >20 keV by decreasing the line-of-sight column density, and the scattering component dominates the spectra at energy below ∼4 keV by artificially increasing $f_{\rm s}$.

The discrepancy of $c_{\rm f,tor}$, however, is more complex due to the fact that the reprocessed component is energy dependent with respect to $c_{\rm f,tor}$, as plotted in the bottom right panel of Figure 3, which plots the spectra of the reprocessed component with different combinations of $\theta_{\rm inc}$ and $c_{\rm f,tor}$. For more information about the reprocessed component of the `borus02` model, we plot the `borus02` model predictions while varying different parameters in Appendix A.

Fixing the inclination angle at $\theta_{\rm inc} = 87°$ puts the strongest constraint on the parameters, e.g., $N_{\rm H,l.o.s}$ and $N_{\rm H,tor}$, among other cases. Such a result is caused by the fact that by fixing the inclination angle at $\theta_{\rm inc} = 87°$, the change in other parameters will lead to large variations in the spectrum. For example, in Figure 3, we find that the spectral shape variation is much larger for $\theta_{\rm inc} = 87°$ than for $\theta_{\rm inc} = 60°$ when $N_{\rm H,tor}$ varies; thus, the uncertainty of $N_{\rm H,tor}$ is much less when using $\theta_{\rm inc} = 87°$ than when using $\theta_{\rm inc} = 60°$. However, the $c_{\rm f,tor}$-related spectral variation is energy dependent in both the $\theta_{\rm inc} = 87°$ and $\theta_{\rm inc} = 60°$ cases; therefore, the average uncertainties of $c_{\rm f,tor}$ are similar in the two cases.

4.4. Distribution of the Obscuring Material

In Sections 4.1–4.3, we discussed how varying the inclination angle affects the measurement of the other spectral parameters of AGNs. Thanks to the flexible and powerful `borus02` model, we could explore a larger parameter space in

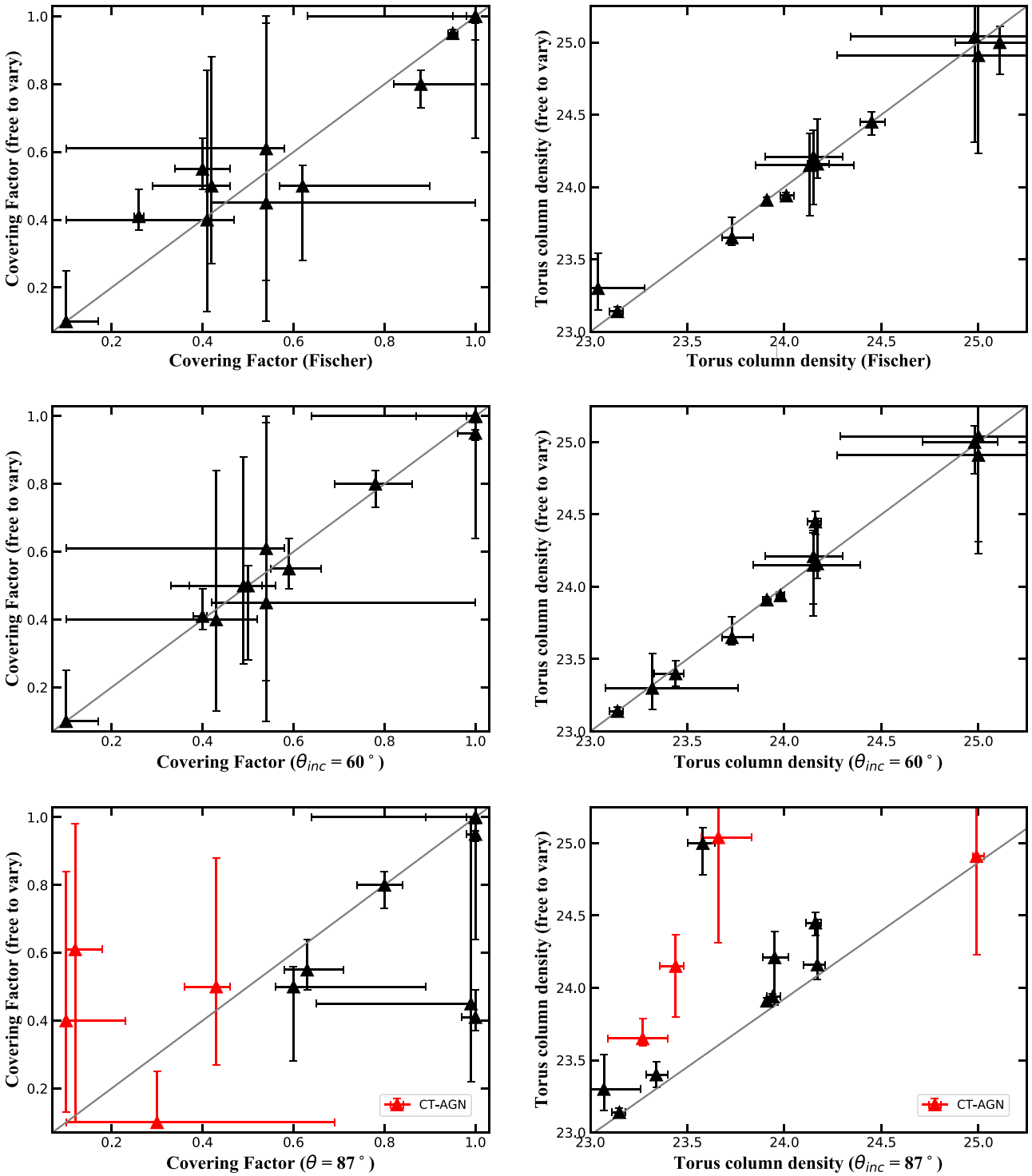

Figure 2. The figures from the left to right in different rows are the $c_{\rm f,tor}$ and $N_{\rm H,tor}$ best-fit values obtained when $\theta_{\rm inc}$ is left free to vary with respect to those obtained when $\theta_{\rm inc}$ is fixed at [O III] measured values (first row), when $\theta_{\rm inc}$ is fixed at $\theta_{\rm inc} = 60^{\circ}$ (second row), and $\theta_{\rm inc} = 87^{\circ}$ (third row), where the gray solid line represents the 1:1 result. CT-AGNs are plotted in red in the third row.

modeling the spectra of AGNs, e.g., we could now directly measure the average column density and the covering factor of the obscuring torus in AGNs. Therefore, in this section, we focus on the correlations among different physical and geometrical properties of the sources in our sample.

A corner plot is drawn in Figure 4 to explore the correlation among different parameters, i.e., line-of-sight column density, $\log(N_{\rm H,l.o.s})$, torus column density, $\log(N_{\rm H,tor})$, torus covering factor, $c_{\rm f}$, 2–10 keV intrinsic luminosity, $L_{\rm int,2-10}$, and Eddington ratio,[9] $\lambda_{\rm Edd}$. Kendall's tau tests are performed for

[9] The Eddington ratio is calculated by $\lambda_{\rm Edd} \equiv L_{\rm bol}/L_{\rm Edd}$, where $L_{\rm bol}$ is the bolometric luminosity. Bolometric luminosity is calculated by $L_{\rm bol} = \kappa\, L_{\rm int,2-10}$, assuming a bolometric correction $\kappa = 20$ (Vasudevan et al. 2010). Eddington luminosity is calculated as $L_{\rm Edd} = 4\pi G M_{\rm BH} m_p c/\sigma_T$, where $M_{\rm BH}$ is the mass of an SMBH and m_p is the mass of proton.

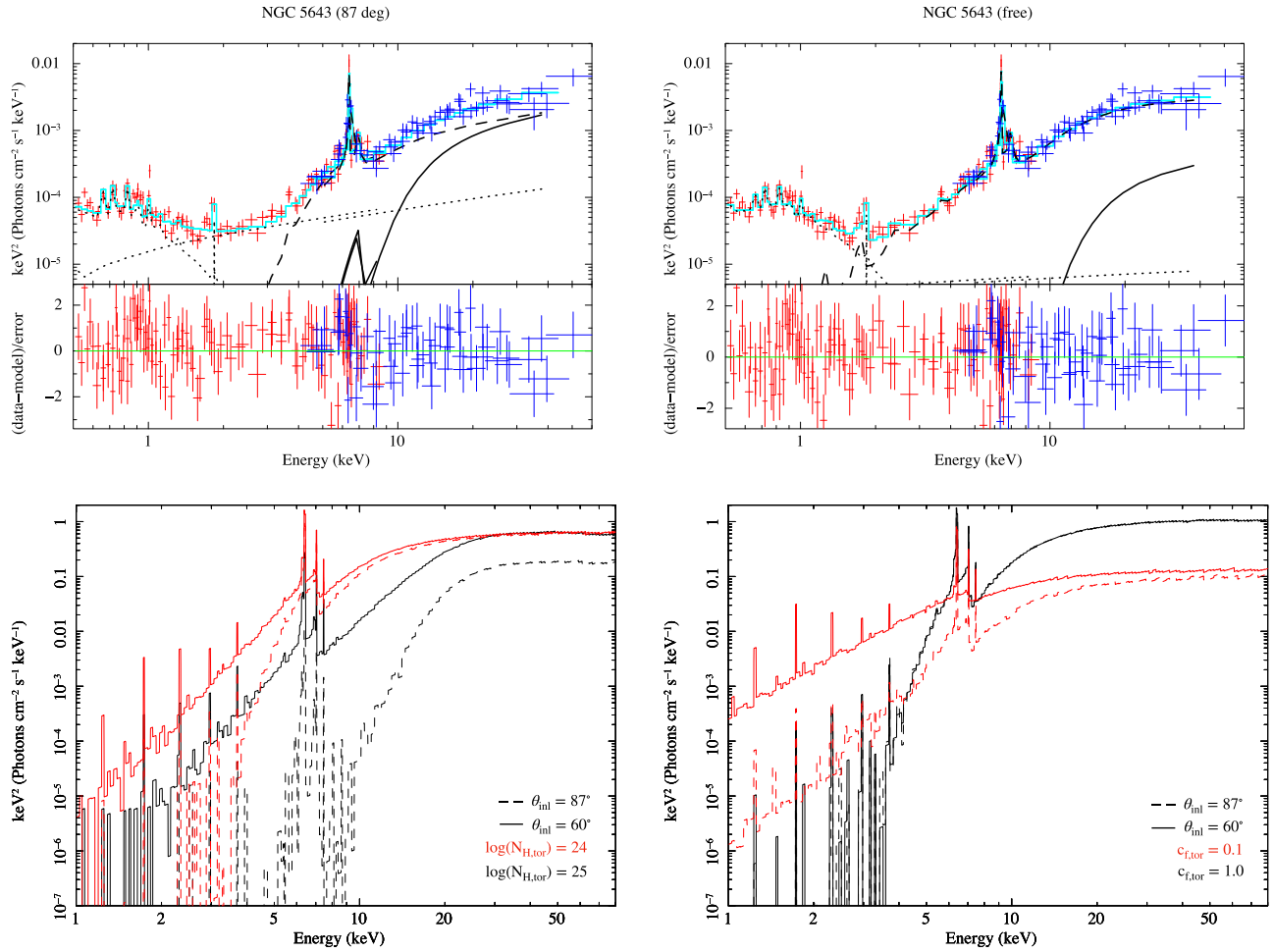

Figure 3. Illustrative example of how fixing the inclination angle at $\theta_{\rm inc} = 87°$ gives very different best-fit results compared to when the inclination angle is left free to vary in fitting the spectra and when the inclination angle is fixed at $\theta_{\rm inc} = 60°$. Top panels: unfolded spectra of NGC 5643 with inclination angle fixed at $\theta_{\rm inc} = 87°$ (left panel) and inclination angle left free to vary (right panel). The NuSTAR data are plotted in blue, and the XMM-Newton data are plotted in red. The best-fit model prediction is plotted as cyan solid lines. The single components of the model are plotted in black with different line styles, i.e., the absorbed intrinsic continuum with solid lines, the reflection component with dashed lines, the scattered component, the `mekal` component, and emission lines with dotted lines. Bottom panels: `borus02` model predictions of the reprocessed component when the inclination angle is fixed at $\theta_{\rm inc} = 87°$ (dashed line) and $\theta_{\rm inc} = 60°$ (solid line). Left bottom panel: the model predictions for $\log(N_{\rm H,tor}) = 24$ (red) and $\log(N_{\rm H,tor}) = 25$ (black); a photon index with $\Gamma = 1.8$ and torus covering factor with $c_{\rm f,Tor} = 0.6$ are assumed. Right bottom panel: the model predictions for $c_{\rm f,Tor} = 0.1$ (red) and $c_{\rm f,Tor} = 1.0$ (black); a photon index with $\Gamma = 1.8$ and torus column density with $\log(N_{\rm H,tor}) = 24$ are assumed.

each pair of parameters and are labeled in each subplot. The best-fit values used are obtained when the inclination angle is left free to vary in fitting the spectra. We also plot the inclination angle as a function of the other properties in Appendix B to explore the correlation between the inclination angle and other properties of the sources.

1. We find no correlation between the measured AGN inclination angle and the other physical and geometrical properties of the AGN as show in Figure B1. Such a result is reasonable since the sources are randomly observed, and the properties of the sources should not be related to the angle at which they are observed.
2. We find no correlations between intrinsic luminosity and torus column density ($p = 0.68$), torus column density and line-of-sight column density ($p = 0.31$), intrinsic luminosity and line-of-sight column density ($p = 0.25$), Eddington ratio and 2–10 keV intrinsic luminosity ($p = 0.25$), and torus covering factor and torus column density ($p = 0.22$).
3. We find a correlation at the confidence level $\sim 2.9\sigma$ between the line-of-sight column density and Eddington ratio ($p = 0.004$), i.e., as the line-of-sight column density increases, the Eddington ratio also increases. We also find an inverse correlation at the confidence level $\sim 2\sigma$ between the line-of-sight column density and torus covering factor ($p = 0.05$), i.e., as the line-of-sight column density increases, the torus covering factor decreases. However, such trends are less evident if we exclude the sources that have been observed to be variable due to the shift of line-of-sight column density, which are marked as gray in Figure 4 from our analysis. The p values become $p = 0.07$ for line-of-sight column density and Eddington ratio and $p = 0.22$ for line-of-sight column density and torus covering factor. Therefore, we are not able confirm the correlation found between line-of-sight column density and Eddington ratio and the inverse correlation between the line-of-sight column density and torus covering factor.

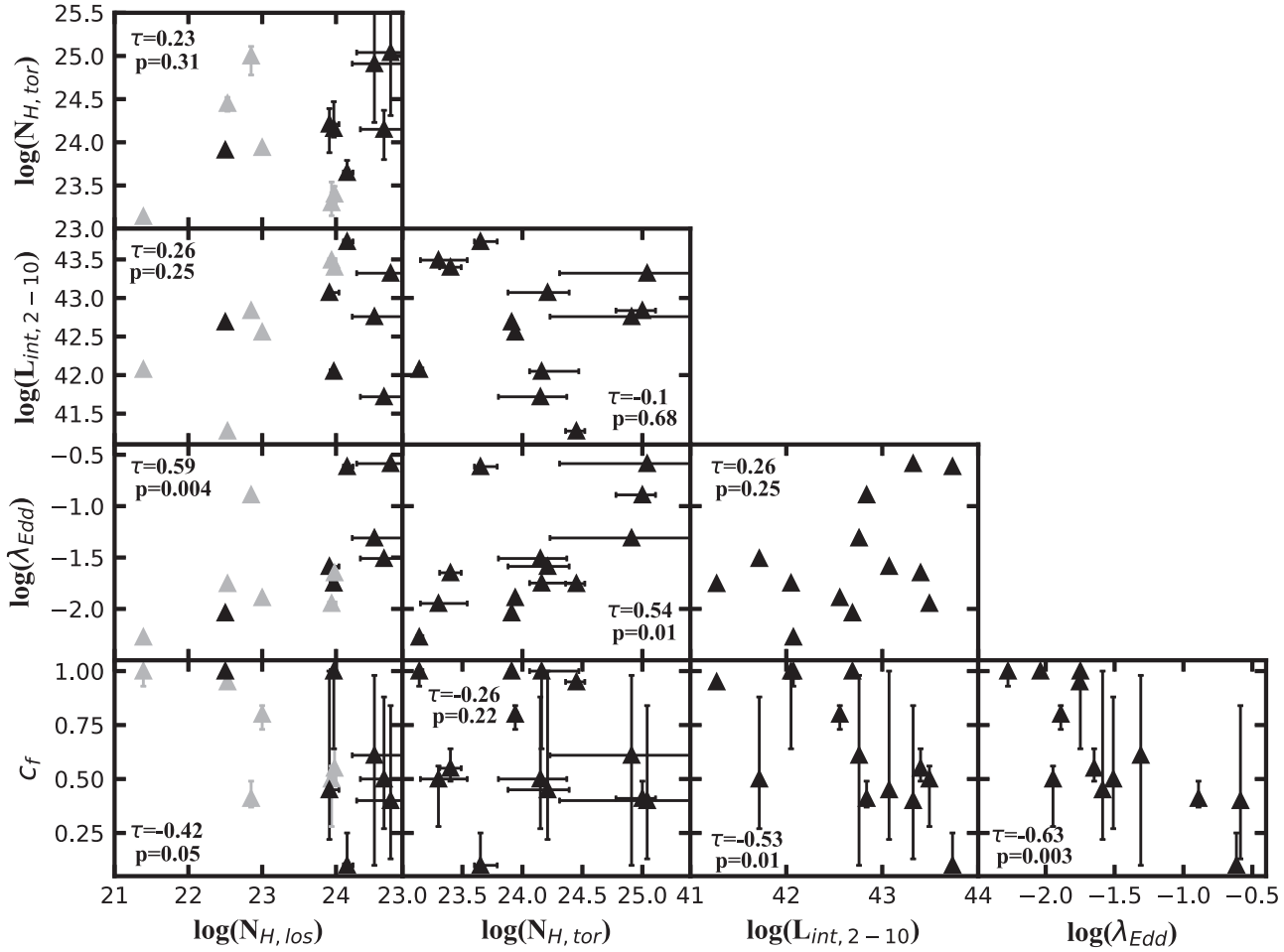

Figure 4. Best-fit results of different parameters, i.e., line-of-sight column density, $N_{\rm H,los}$, torus column density, $N_{\rm H,tor}$, torus covering factor, $c_{\rm f}$, 2–10 keV intrinsic luminosity, $L_{\rm int,2-10}$, and Eddington ratio, $\lambda_{\rm Edd}$, as a function of each other. Sources with known line-of-sight column density variability are plotted in gray. The tau values and p values in the Kendalls tau test are computed for each pair of parameters and are also labeled in each subplot.

4. We find a correlation at the confidence level $\sim 2.6\sigma$ between the 2 and 10 keV intrinsic luminosity and the torus covering factor ($p = 0.01$), i.e., as the intrinsic luminosity increases, the torus covering factor decreases. Such a trend has been reported in many previous works with larger samples and higher statistical accuracy in different redshift ranges (e.g., Lawrence & Elvis 1982; Hasinger 2008; Ueda et al. 2014). The covering factor of the torus in these works is derived from the X-ray hardness ratio or the fraction of the obscured Compton thin sources ($22 \leqslant \log(N_{\rm H}) \leqslant 24$) in these works. A similar trend has also been found by Baloković (2017), who measured the individual torus covering factors and their intrinsic luminosities as in this work.
5. We find an inverse correlation at the confidence level $\sim 3\sigma$ between the Eddington ratio and torus covering factor ($p = 0.003$), i.e., as the Eddington ratio of the AGN increases, the covering factor of the obscuring torus decreases. We also find a correlation at the confidence level $\sim 2.6\sigma$ between the Eddington ratio and torus column density ($p = 0.01$), i.e., as the Eddington ratio of the AGN increases, the average column density of the obscuring torus decreases. Such results are in good agreement with those reported in Ricci et al. (2017), who found that the torus covering factor and the torus average column density strongly depend on the Eddington ratio of the AGN using a larger BAT selected sample of 392 AGNs. The dependence of torus covering factor and torus average column density on the Eddington ratio can be explained assuming that the distribution of the circumnuclear material around the SMBH is mainly regulated by the radiative feedback: as the accretion rate increases, the radiation pressure from the accretion disk blows the less dense ($\log(N_{\rm H}) \leqslant 24$) materials away and leaves only the CT materials, thus decreasing the torus covering factor and increasing the torus average column density (Fabian et al. 2006, 2009; Ricci et al. 2017). We point out that in Ricci et al. (2017), the covering factors are indirectly measured, using the fraction of obscured ($22 \leqslant \log(N_{\rm H})$) AGNs with respect to all AGNs with $20 \leqslant \log(N_{\rm H})$ in their sample. To better visualize the above correlations, we display the best-fit torus covering factors as a function of their measured Eddington ratio and the best-fit torus column densities as a function of their measured Eddington ratio separately in Figure 5. To compare with the results obtained in Ricci et al. (2017), we rebin our results in plotting the torus covering factors as a function of Eddington ratio. We find that our average torus covering factor is in good agreement with that of Ricci et al. (2017), especially at large Eddington ratios.

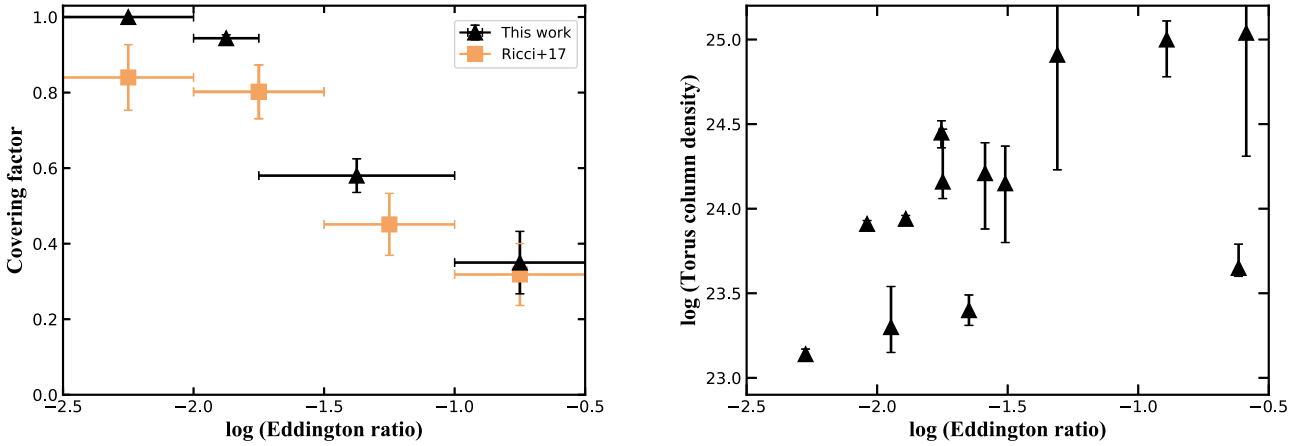

Figure 5. Left panel: torus covering factors as a function of the Eddington ratio of the 13 sources, which are rebinned to compare with the torus covering factor and Eddington ratio relationship measured in Ricci et al. (2017; shown here as orange squares). The results are rebinned to make sure that each bin has similar number of sources. Right panel: torus column densities as a function of the Eddington ratio of the 13 sources.

The fact that no correlation is found between 2 and 10 keV intrinsic luminosity and torus average column density, together with the correlations found between torus covering factor and torus average column density with respect to the Eddington ratio, suggests that the distribution of the obscuring materials surrounding the SMBH of the AGNs in our sample is mainly regulated by the Eddington ratio rather than the intrinsic luminosity, which is in agreement with what is found in Ricci et al. (2017). Nevertheless, the distribution of the materials in the obscuring torus in AGNs needs to be further studied in a larger unbiased sample with high-quality spectra.

4.5. Geometrical Properties of Torus and NLR

According to the unified model, the dusty torus obscures the radiation from the center engine of the AGN and is therefore thought to form the biconical shape of the NLR or the ionization cone (Malkan et al. 1998). Fischer et al. (2013) report the opening angle of the outer edge of the NLR obtained by modeling the kinematics of the sources' NLR observed with the HST and the STIS. In this section, we explore the relation between the geometrical properties of the AGNs in our sample measured in optical and measured in X-ray.

In Figure 6, we plot the covering factor of the region excluding the NLR measured in optical, i.e., $1 - c_{\rm f,NLR}$, as a function of the covering factor of the torus measured in X-ray, i.e., $c_{\rm f,Tor}$. We find that: (1) there is no correlation between $c_{\rm f,tor}$ and $1 - c_{\rm f,NLR}$ ($\tau = 0.18$ and $p = 0.42$); (2) while $c_{\rm f,Tor}$ span all values from 0.1 to 1, $c_{\rm f,NLR}$ does not (i.e., $c_{\rm f,NLR} < 0.5$). However, our results may be biased by the fact that: `borus02` assumes a uniformly distributed obscuring material scenario; therefore, the $c_{\rm f,Tor}$ measured in `borus02` is the effective fraction of the sky that is covered by the obscuring material, which thus gives the lower limit of the realistic clumpy $c_{\rm f,Tor}$; the optical emission associated with the NLR measured by Fischer et al. (2013) may contain the emission from a star formation process, which might lead to inaccurate measurement of the geometry of the NLR. Therefore, further studies with a larger sample of AGNs with multiwavelength data sets are needed to understand the geometrical properties of the different components of the AGN.

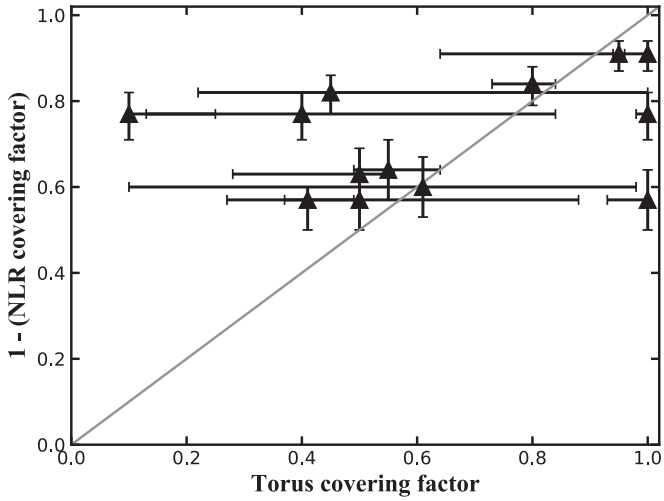

Figure 6. Relationship between the covering factor of the region excluding the NLR, i.e., $1 - c_{\rm f,NLR}$, with respect to the covering factor of the torus, i.e., $c_{\rm f,Tor}$. The gray solid line represents the 1:1 result.

5. Conclusion

We performed a broadband X-ray spectral analysis on a sample of AGNs selected from Fischer et al. (2013) with [O III] measured inclination angle, using high-quality NuSTAR, XMM-Newton, and Chandra archival data. To model the spectra, we utilized the recently published self-consistent `borus02` model, which is effective in characterizing the physical and geometrical properties of the obscuring materials near the SMBH. The main findings of this work are reported as follows.

1. The best-fit values of the spectral parameters obtained when the sources are fitted with the inclination angle fixed at the [O III] measured values are similar to those obtained when the inclination angle is left free to vary. Fixing the inclination angle at $\theta_{\rm inc} = 60°$ also gives similar spectral fit results, but incorrect fit results may be obtained for some CT sources out of our sample. Fixing the inclination angle at $\theta_{\rm inc} = 87°$ leads to significantly different measurements of the torus covering factor and

the torus column density even for CT-AGNs, but it gives the best constraints on different parameters.

2. In AGN X-ray spectral analysis, one should always leave the inclination angle free to vary. If one intends to better constrain the properties of sources when fitting low-quality X-ray spectra (i.e., $\leqslant$300 d.o.f), one should fit the spectra by leaving $\theta_{\rm inc}$ free to vary at first, then fix $\theta_{\rm inc}$ at some reasonable values, e.g., $\theta_{\rm inc} = 60^{\circ}$ or [O III] measured values. Comparing the best-fit results of the two methods: only when the best-fit values of all parameters fitted when fixing the $\theta_{\rm inc}$ are in good agreement with those obtained when leaving $\theta_{\rm inc}$ free to vary in fitting the spectra could one fix $\theta_{\rm inc}$ at those values; otherwise, fixing $\theta_{\rm inc}$ at preferred values should always be avoided, and $\theta_{\rm inc}$ should be left free to vary in fitting these spectra.
3. The properties of AGNs in our sample are not dependent on the direction at which they are observed, i.e., the inclination angle.
4. We confirm a strong inverse correlation between the torus covering factor and the Eddington ratio, and a correlation between the torus average column density and the Eddington ratio measured in the sources of our sample, which is in good agreement with the radiative feedback model. We also find an inverse correlation between the torus covering factor and the 2–10 keV intrinsic luminosity, which has also been measured in previous works. However, we do not find any correlation between the torus average column density and the 2–10 keV intrinsic luminosity, suggesting that the distribution of the materials in the obscuring torus is regulated by the Eddington ratio rather than the intrinsic luminosity.
5. We found no geometrical correlation between the two components of AGNs, i.e., the obscuring torus and NLR. The torus covering factors span all values, while the covering factors of the NLR do not. The ability to robustly measure the covering factor of the torus in the X-ray band is currently limited by the data quality, sample size, and the lack of sufficiently realistic spectral models, which we expect to improve in future work. However, this result already suggests that AGN geometry might be more complex than what is assumed in the simplistic unified model of AGNs.

X. Z. thanks the anonymous referee for the detailed and useful comments, which helped to significantly improve this paper. X. Z., S.M., and M.A. acknowledge NASA funding under contracts 80NSSC17K0635 and 80NSSC19K0531. M.B. acknowledges support from the Black Hole Initiative at Harvard University, which is funded in part by the Gordon and Betty Moore Foundation (grant GBMF8273) and in part by the John Templeton Foundation. NuSTAR is a project led by the California Institute of Technology (Caltech), managed by the Jet Propulsion Laboratory (JPL), and funded by the National Aeronautics and Space Administration (NASA). We thank the NuSTAR Operations, Software, and Calibrations teams for support with these observations. This research has made use of the NuSTAR Data Analysis Software (NuSTARDAS) jointly developed by the ASI Science Data Center (ASDC, Italy) and the California Institute of Technology (USA). This research has made use of data and/or software provided by the High Energy Astrophysics Science Archive Research Center (HEASARC), which is a service of the Astrophysics Science Division at NASA/GSFC and the High Energy Astrophysics Division of the Smithsonian Astrophysical Observatory. This work is based on observations obtained with XMM-Newton, an ESA science mission with instruments and contributions directly funded by ESA Member States and NASA.

Appendix A
`borus02` Model

We plot the spectra of the `borus02` model prediction of the reprocessed component when varying different parameters, i.e., torus covering factor, $c_{\rm f,tor}$, inclination angle, $\theta_{\rm inc}$, torus column density, $N_{\rm H,tor}$, and relative iron abundance, $A_{\rm Fe}$, in Figure A1.

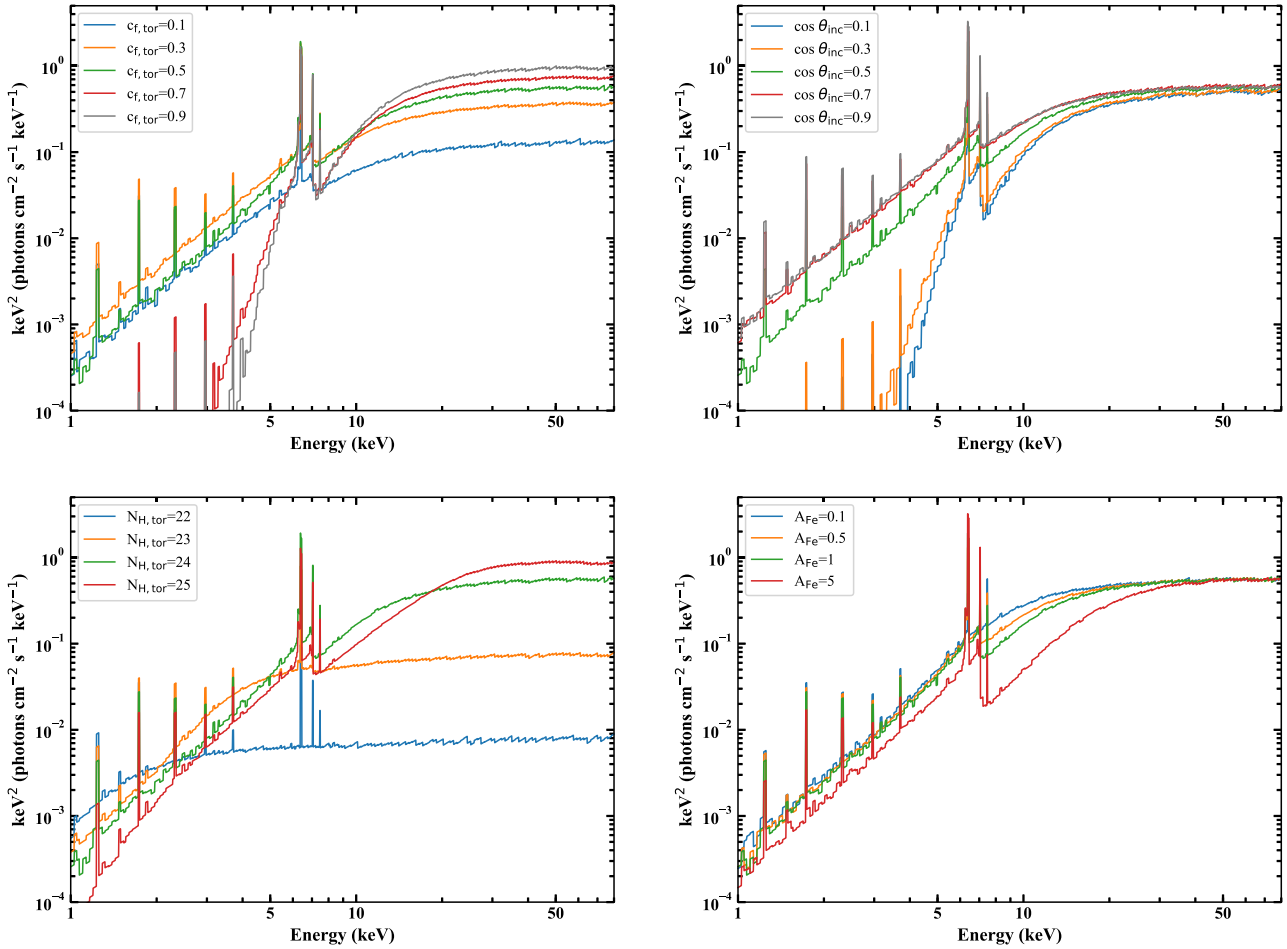

Figure A1. Top left panel: spectra of the `borus02` (Baloković et al. 2018) model prediction of the reprocessed component with varying $c_{f,tor}$, assuming $\cos(\theta_{inc}) = 0.5$, $\log(N_{H,tor}) = 24$, and $A_{Fe} = 1$. Top right panel: spectra of the `borus02` model prediction of the reprocessed component with varying θ_{inc}, assuming $c_{f,tor} = 0.5$, $\log(N_{H,tor}) = 24$, and $A_{Fe} = 1$. Bottom left panel: spectra of the `borus02` model prediction of the reprocessed component with varying $N_{H,tor}$, assuming $c_{f,tor} = 0.5$, $\cos(\theta_{inc}) = 0.5$, and $A_{Fe} = 1$. Bottom right panel: spectra of the `borus02` model prediction of the reprocessed component with varying A_{Fe}, assuming $c_{f,tor} = 0.5$, $\cos(\theta_{inc}) = 0.5$, and $\log(N_{H,tor}) = 24$. All spectra assumed a $\Gamma = 1.8$.

Appendix B
Dependence of the Properties of AGNs on Their Inclinations

We plot the best-fit inclination angle of the 13 sources in our sample as a function of their line-of-sight column density, torus covering factor, torus column density, Eddington ratio, and 2–10 keV intrinsic luminosity in Figure B1. The tau and p values for each pair of properties are calculated and reported in each subplot. We find no correlation between the measured inclination angle of AGNs and the other physical and geometrical properties of AGNs.

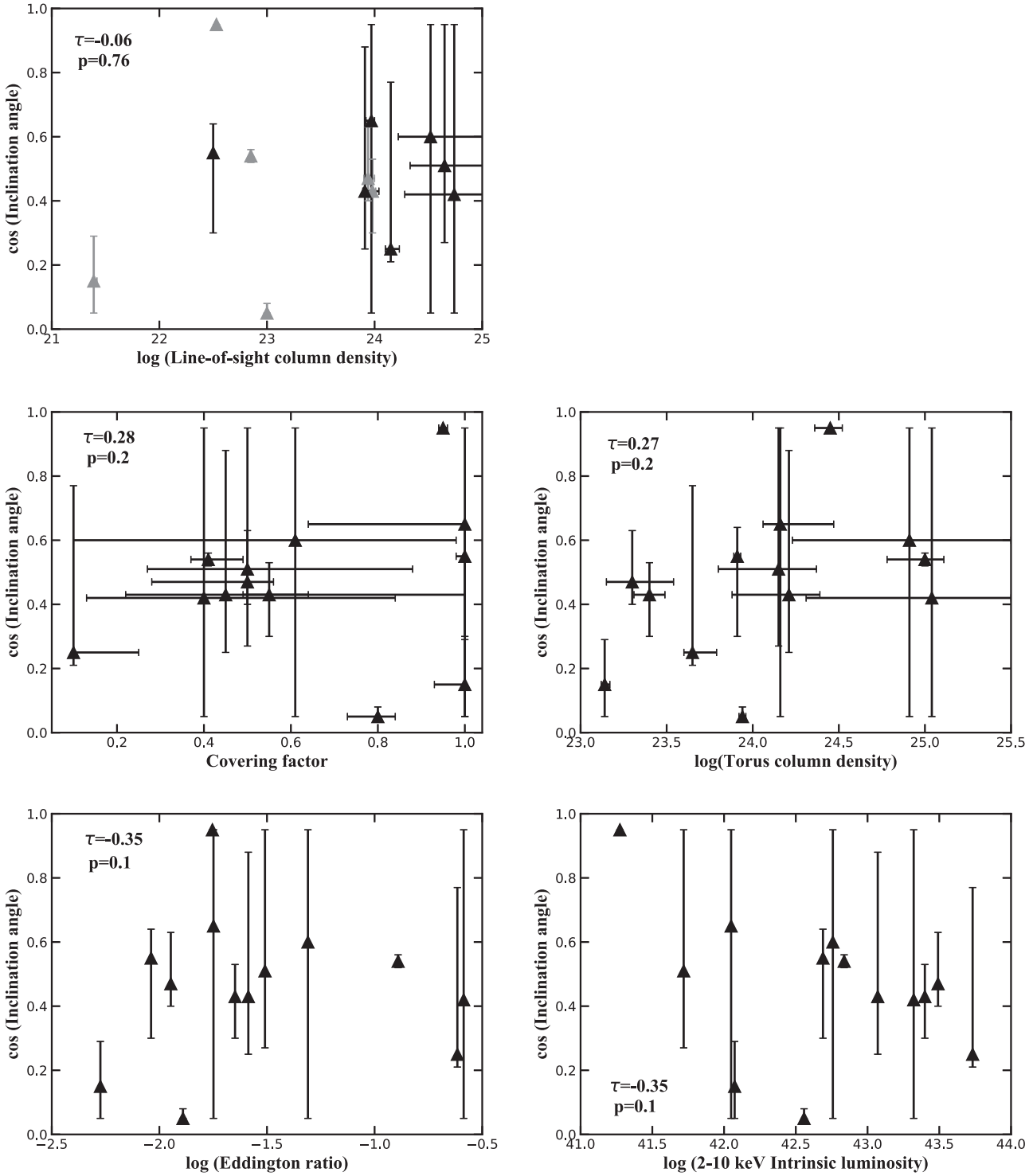

Figure B1. Best-fit inclination angle of the 13 sources in our sample as a function of their line-of-sight column density, torus covering factor, torus column density, Eddington ratio, and 2–10 keV intrinsic luminosity. The tau and p values for each pair of properties are calculated and reported in each subplot. Sources that have been observed to be variable due to the variability of line-of-sight column density are marked in gray.

Appendix C
Fitting Details and Spectra of the 13 Sources

C.1. Fitting Details

Mrk 3: the cutoff energy $E_{\rm cut}$ of the source is found to be much less than the default 500 keV; thus, we leave $E_{\rm cut}$ free to vary in fitting the spectra of Mrk 3, and $E_{\rm cut} = 85^{+55}_{-20}$ keV is measured. The relative iron abundance is found to be less than the default value; thus, the relative iron abundance is left free to vary in fitting the spectrum of Mrk 3, and $A_{\rm Fe} = 0.44^{+0.14}_{-0.08}\ A_{\rm Fe,\odot}$ is measured. The best-fit statistic of the scenario of leaving $\theta_{\rm inc}$ free to vary is χ^2/degree of freedom (d.o.f) $= 1056/1073 \approx 0.98$. The best-fit photon index for Mrk 3 is $\Gamma = 1.48^{+0.11}_{-u}$, where u means the parameter cannot be constrained at the 90% confidence level within the range of the parameter in the `borus02` model, which is [1.4–2.6] for Γ. The best-fit line-of-sight column density is

$\log(N_{\rm H,l.o.s}) = 23.94^{+0.06}_{-0.04}$, and the best-fit torus column density is $\log(N_{\rm H,tor}) = 23.30^{+0.24}_{-0.15}$. The best-fit inclination angle is $\cos(\theta_{\rm inc}) = 0.47^{+0.16}_{-0.07}$, and the best-fit covering factor is $c_{\rm f,tor} = 0.50^{+0.06}_{-0.22}$.

Mrk 34: an energy range of 0.6–78 keV rather than 0.5–78 keV is used in fitting the spectrum of Mrk 34 since we found that the spectrum between 0.5 and 2 keV cannot be fitted by a single `mekal` model; however, the spectrum between 0.6 and 2 keV can be well fitted by a single `mekal` model. In addition, we added a number of unresolved Gaussian lines as needed to reach a good fit of Mrk 34. The best-fit statistic of Mrk 34 is $\chi^2/{\rm d.o.f} = 74/82 \approx 0.90$. The best-fit photon index is $\Gamma = 1.45^{+0.67}_{-u}$. The best-fit line-of-sight column density is $\log(N_{\rm H,l.o.s}) > 24.28$ and the best-fit torus column density is $\log(N_{\rm H,tor}) = 25.04^{+u}_{-0.73}$, where the parameter range of $\log(N_{\rm H,tor})$ in `borus02` table is [22.0–25.5]. The best-fit inclination angle is $\cos(\theta_{\rm inc}) = 0.42^{+u}_{-u}$, suggesting that the inclination angle of Mrk 34 is unconstrained with current data. The best-fit covering factor of Mrk 34 is $c_{\rm f,tor} = 0.40^{+0.44}_{-0.27}$.

Mrk 78: We adopted NuSTAR data from 4 to 78 keV since the NuSTAR data between 3 and 4 keV showed strong discrepancy with XMM-Newton and Chandra data. We found a strong emission line at ∼8.265 keV in the spectrum, which belongs to the Ni Kβ emission line. Thus, a Gaussian line centered at $E_l = 8.265$ keV with zero width is added to better fit the spectrum. We compare the flux of the Ni Kβ emission line and Fe Kα line: the measured flux of the Fe Kα line of Mrk 78 is $F_{\rm lux,Fe\ K\alpha} = 4.5 \times 10^{-15}\,{\rm erg\,cm^{-2}\,s^{-1}}$ between 6.39 and 6.41 keV, and the measured flux of the Ni Kβ line is $F_{\rm lux,Ni\ K\beta} = 3.8 \times 10^{-15}\,{\rm erg\,cm^{-2}\,s^{-1}}$ between 8.255 and 8.275 keV. Strong variability is also found between the NuSTAR observations and the three soft X-ray observations. The 2–10 keV flux of Mrk 78 observed in NuSTAR increased by ∼135% with respect to the flux observed in XMM-Newton. We found that the variability observed in Mrk 78 is caused by both the variability of intrinsic emission and $N_{\rm H,l.o.s}$ variability. The intrinsic emission of Mrk 78 measured using the NuSTAR observations increased by ∼38% with respect to the intrinsic emission measured using XMM-Newton observations, and the $N_{\rm H,l.o.s}$ observed in NuSTAR decreased by 49% with respect to the $N_{\rm H,l.o.s}$ observed in XMM-Newton, i.e., $\log(N_{\rm H,l.o.s,NuS}) = 23.62^{+0.08}_{-0.08}$ from $\log(N_{\rm H,l.o.s,XMM}) = 23.91^{+0.13}_{-0.02}$. The best-fit statistic of Mrk 78 is $\chi^2/{\rm d.o.f} = 276/271 \approx 1.02$. The best-fit photon index of Mrk 78 is $\Gamma = 1.40^{+0.21}_{-u}$. The best-fit torus column density is $\log(N_{\rm H,tor}) = 24.21^{+0.18}_{-0.33}$. The best-fit inclination angle is $\cos(\theta_{\rm inc}) = 0.43^{+0.45}_{-0.18}$, and the best-fit covering factor is found to be $c_{\rm f,tor} > 0.22$.

Mrk 573: an energy range of 0.3–78 keV rather than 0.5–78 keV is used in fitting the spectrum of Mrk 573 because we found that the spectrum of Mrk 573 between 0.5 and 2 keV cannot be fitted by a single `mekal` model. Although the spectrum between 0.8 and 2 keV can be fitted by a single `mekal` model, to exploit the high-quality XMM-Newton data below 0.8 keV, which provide ∼2600 more counts (the total counts in the spectra between 0.8 and 78 keV are ∼2400 cts), we fit the spectra of Mrk 573 in the 0.3–78 keV energy band and add another `mekal` in our modeling. The best-fit statistic of Mrk 573 is $\chi^2/{\rm d.o.f} = 152/194 \approx 0.78$. The best-fit photon index is $\Gamma = 2.35^{+u}_{-0.65}$. The best-fit line-of-sight column density is $\log(N_{\rm H,l.o.s}) > 24.22$, and the best-fit average torus column density is $\log(N_{\rm H,tor}) > 24.23$. The best-fit inclination angle is $\cos(\theta_{\rm inc}) = 0.60^{+u}_{-u}$, and the best-fit torus covering factor is $c_{\rm f,tor} < 0.98$, suggesting that we are unable to constrain both the inclination and the torus covering factor of Mrk 573.

Mrk 1066: the cutoff energy $E_{\rm cut}$ of Mrk 1066 is found to be $E_{\rm cut} < 28$ keV. The relative iron abundance is found to be $A_{\rm Fe} = 3.2^{+0.7}_{-1.0}\ A_{\rm Fe,\odot}$. In addition, we added a number of unresolved Gaussian lines as needed to reach a good fit of Mrk 1066. The best-fit statistic of Mrk 1066 is $\chi^2/{\rm d.o.f} = 142/147 \approx 0.97$. The best-fit photon index is $\Gamma = 1.52^{+0.02}_{-u}$. The best-fit line-of-sight column density is $\log(N_{\rm H,l.o.s}) = 23.97^{+0.03}_{-0.05}$, and the best-fit average torus column density is $\log(N_{\rm H,tor}) = 24.16^{+0.31}_{-0.10}$. The best-fit inclination angle is $\cos(\theta_{\rm inc}) = 0.65^{+u}_{-u}$, suggesting that the inclination angle of Mrk 1066 is fully unconstrained with current data. The best-fit covering factor is $c_{\rm f,tor} > 0.64$.

NGC 3227: the source is found to be an unobscured AGN with $N_{\rm H,l.o.s} < 10^{22}\,{\rm cm^{-2}}$. We found that the scattering component contributes marginally to the spectrum, and abandon of this component does not worsen the fit. Therefore, we set the fraction of the scattering component to be $f_s = 0$ to decrease the free parameters in fitting. The spectra below 1 keV have no obvious emission signatures and are difficult to be well fitted by `mekal`. We add a phenomenological Gaussian and an unabsorbed cutoff power law with a different photon index to fit the soft X-ray spectrum of NGC 3227. The center of the Gaussian is at $E_l = 0.62$ keV, and the width is $\sigma = 0.05$ keV. The photon index of this phenomenological cutoff power law is measured as $\Gamma_{\rm soft} = 3.9^{+0.1}_{-0.1}$ compared to the best-fit photon index of the intrinsic cutoff power law of $\Gamma = 1.68^{+0.01}_{-0.01}$. The best-fit statistic of NGC 3227 is $\chi^2/{\rm d.o.f} = 4684/4008 \approx 1.17$. The best-fit line-of-sight column density is $\log(N_{\rm H,l.o.s}) = 21.39^{+0.03}_{-0.01}$, and the best-fit average torus column density is $\log(N_{\rm H,tor}) = 23.14^{+0.03}_{-0.02}$. The best-fit inclination angle is $\cos(\theta_{\rm inc}) < 0.29$, and the best-fit covering factor is $c_{\rm f,tor} > 0.93$.

NGC 3783: NuSTAR data above 70 keV are polluted by background noise, and the data <10 keV show a strong discrepancy with XMM-Newton, so we fit the NuSTAR spectrum only between 10 and 70 keV following the approach adopted in previous works (Mehdipour et al. 2017; Mao et al. 2019; de Marco et al. 2020). The cutoff energy $E_{\rm cut}$ of NGC 3783 is found to be $E_{\rm cut} = 37^{+2}_{-4}$ keV. In addition, we added a number of unresolved Gaussian lines as needed to reach a good fit of Mrk 3783. The best-fit statistic of NGC 3783 is $\chi^2/{\rm d.o.f} = 3349/2929 \approx 1.14$. The best-fit photon index is $\Gamma = 1.51^{+0.02}_{-0.04}$. The best-fit line-of-sight column density is $\log(N_{\rm H,l.o.s}) = 22.85^{+0.01}_{-0.01}$, and the best-fit average torus column density is $\log(N_{\rm H,tor}) = 25.00^{+0.11}_{-0.22}$. The best-fit inclination angle is $\cos(\theta_{\rm inc}) = 0.54^{+0.02}_{-0.02}$, and the best-fit covering factor is $c_{\rm f,tor} = 0.41^{+0.08}_{-0.04}$.

NGC 4051: the source is known to exhibit strong spectra and flux variation in X-ray (Turner et al. 2017). Variability is also found between the NuSTAR and XMM-Newton observations that we analyzed. The 2–10 keV flux of the NuSTAR observation is ∼24% less than the XMM-Newton observation. This flux variability is caused by the variability of the intrinsic emission rather than the $N_{\rm H,l.o.s}$ variability based our analysis. The source is also known to possess a warm absorber outflow (Mizumoto & Ebisawa 2016), due to its absorption signature, especially the $O_{\rm VIII}$ absorption feature ∼0.65 keV, which is difficult to be fitted by the default `mekal` model. We tried to use a complex phenomenological model to fit the spectrum below 1 keV and found that the best-fit results of the key parameters

did not vary compared with those obtained when we fitted the spectra only above 1 keV. Therefore, we fit the spectra of NGC 4051 with energy only above 1 keV. The cutoff energy $E_{\rm cut}$ of NGC 4051 is found to be $E_{\rm cut} = 44^{+2}_{-2}$ keV. The best-fit statistic of NGC 4051 is $\chi^2/{\rm d.o.f} = 2686/2389 \approx 1.12$. The best-fit photon index is $\Gamma = 1.72^{+0.01}_{-0.01}$. The best-fit line-of-sight column density is $\log(N_{\rm H,l.o.s}) = 22.53^{+0.01}_{-0.01}$, and the best-fit average torus column density is $\log(N_{\rm H,tor}) = 24.45^{+0.07}_{-0.09}$. The best-fit inclination angle is $\cos(\theta_{\rm inc}) > 0.94$, and the best-fit covering factor is $c_{\rm f,tor} = 0.95^{+0.01}_{-0.01}$.

NGC 4151: the source is known to exhibit spectral and flux variability in X-ray (Beuchert et al. 2017). Strong variability was also found between the NuSTAR and XMM-Newton observations in our analysis. The 2–10 keV flux of the NuSTAR observations is ∼103% larger than that of the XMM-Newton observations. This flux variability is caused by both the variability of the intrinsic emission and the $N_{\rm H,l.o.s}$ variability based on our analysis. The intrinsic emission measured using NuSTAR observations is ∼80% larger than the intrinsic emission measured using XMM-Newton observations. The line-of-sight column densities of the two observations are $\log(N_{\rm H,l.o.s,NuS}) = 22.86^{+0.02}_{-0.01}$ and $\log(N_{\rm H,l.o.s,XMM}) = 23.00^{+0.01}_{-0.01}$, respectively. The cutoff energy $E_{\rm cut}$ of NGC 4151 is found to be $E_{\rm cut} = 112^{+10}_{-16}$ keV. The relative iron abundance is found to be $A_{\rm Fe} = 0.66^{+0.05}_{-0.05}\ A_{\rm Fe,\odot}$ when the inclination is fixed at [O III] measured value in fitting. In addition, we added a number of unresolved Gaussian lines as needed to reach a good fit of NGC 4151. The best-fit statistic of NGC 4151 is $\chi^2/{\rm d.o.f} = 5200/4664 \approx 1.11$. The best-fit photon index of NGC 4151 is $\Gamma = 1.67^{+0.02}_{-0.04}$. The best-fit average torus column density is $\log(N_{\rm H,tor}) = 23.94^{+0.02}_{-0.02}$. The best-fit inclination angle is $\cos(\theta_{\rm inc}) < 0.08$, and the best-fit covering factor is $c_{\rm f,tor} = 0.80^{+0.04}_{-0.07}$.

NGC 4507: the source is known to exhibit spectral and flux variability in X-ray (Braito et al. 2012; Marinucci et al. 2013). Variability was also found between the NuSTAR and XMM-Newton observations in our analysis. The 2–10 keV flux of the NuSTAR observations is ∼51% larger than that of the XMM-Newton observations. This flux variability is caused by the variability of the intrinsic emission rather than the $N_{\rm H,l.o.s}$ variability based on our analysis. The intrinsic emission measured using NuSTAR observations is 50% larger than the intrinsic emission measured using XMM-Newton observations. The spectrum below 1 keV is difficult to model with a single `mekal`, so we add another `mekal` in fitting the spectrum. The relative iron abundance is found to be $A_{\rm Fe} = 0.5^{+0.1}_{-0.1}\ A_{\rm Fe,\odot}$. In addition, we added a number of unresolved Gaussian lines as needed to reach a good fit of NGC 4507. The best-fit statistic of NGC 4507 is $\chi^2/{\rm d.o.f} = 1601/1614 \approx 0.99$. The best-fit photon index is $\Gamma = 1.71^{+0.05}_{-0.03}$. The best-fit line-of-sight column density is $\log(N_{\rm H,l.o.s}) = 23.98^{+0.03}_{-0.05}$, and the best-fit average torus column density is $\log(N_{\rm H,tor}) = 23.40^{+0.09}_{-0.09}$. The best-fit inclination angle is $\cos(\theta_{\rm inc}) = 0.43^{+0.10}_{-0.13}$, and the best-fit covering factor is $c_{\rm f,tor} = 0.55^{+0.09}_{-0.06}$.

NGC 5506: the source is known to exhibit spectral and flux variability in X-ray (Sun et al. 2018). Variability was also found between the NuSTAR and XMM-Newton observations that we adopted. The 2–10 keV flux of the NuSTAR observations is ∼18% less than that of the XMM-Newton observations. This flux variability is caused by both the variability of the intrinsic emission and the $N_{\rm H,l.o.s}$ variability based on our analysis. The intrinsic emission measured using NuSTAR is 25% less than the intrinsic emission measured using XMM-Newton observations, and the line-of-sight column densities measured in the two observations are $\log(N_{\rm H,l.o.s,NuS}) = 22.29^{+0.03}_{-0.02}$ and $\log(N_{\rm H,l.o.s,XMM}) = 22.50^{+0.01}_{-0.01}$, respectively. The relative iron abundance is found to be $A_{\rm Fe} = 5.8^{+0.4}_{-0.2}\ A_{\rm Fe,\odot}$. The cutoff energy $E_{\rm cut}$ of NGC 5506 is found to be $E_{\rm cut} < 21$ keV. In addition, we found that the fit was significantly improved (from $\chi^2/{\rm d.o.f} = 5590/4544$ to $\chi^2/{\rm d.o.f} = 5378/4543$) if we leave the photon index of the cutoff power law of the scattering component free to vary. We measured the photon index of the scattering component as $\Gamma_{\rm soft} = 1.02^{+0.30}_{-0.02}$, and the best-fit photon index of the intrinsic emission is $\Gamma = 1.72^{+0.01}_{-0.01}$. The best-fit statistic of NGC 5506 is $\chi^2/{\rm d.o.f} = 5378/4543 \approx 1.18$. The best-fit average torus column density is $\log(N_{\rm H,tor}) = 23.91^{+0.02}_{-0.02}$. The best-fit inclination angle is $\cos(\theta_{\rm inc}) = 0.55^{+0.09}_{-0.25}$, and the best-fit covering factor is $c_{\rm f,tor} > 0.98$.

NGC 5643: a strong emission line at ∼1.836 keV, which belongs to the Si Kβ emission line, is found. Therefore, a Gaussian line with zero width is added to better fit the spectrum. The best-fit statistic of NGC 5643 is $\chi^2/{\rm d.o.f} = 198/170 \approx 1.16$. The best-fit photon index of NGC 5643 is $\Gamma = 1.77^{+0.27}_{-0.37}$. The best-fit line-of-sight column density is $\log(N_{\rm H,l.o.s}) > 24.33$, and the best-fit average torus column density is $\log(N_{\rm H,tor}) = 24.15^{+0.22}_{-0.35}$. The best-fit inclination angle is $\cos(\theta_{\rm inc}) > 0.27$, and the best-fit covering factor is $c_{\rm f,tor} = 0.50^{+0.38}_{-0.23}$.

NGC 7674: the source is known to exhibit spectra and flux variation in X-ray (Gandhi et al. 2017). Variability was also found between the NuSTAR and XMM-Newton observations that we adopted. The 2–10 keV flux of the NuSTAR observations is ∼29% larger than that of the XMM-Newton observations. This flux variability is caused by both the variability of the intrinsic emission and the $N_{\rm H,l.o.s}$ variability according to our analysis. The intrinsic emission measured using NuSTAR observations is 113% larger than the intrinsic emission measured using XMM-Newton observations, and the line-of-sight column densities measured in the two observations are $\log(N_{\rm H,l.o.s,NuS}) = 24.45^{+0.05}_{-0.02}$ and $\log(N_{\rm H,l.o.s,XMM}) = 24.15^{+0.08}_{-0.05}$, respectively. The relative iron abundance is found to be $A_{\rm Fe} = 0.42^{+0.09}_{-0.08}\ A_{\rm Fe,\odot}$. The best-fit statistic of NGC 7674 is $\chi^2/{\rm d.o.f} = 240/251 \approx 0.96$. The best-fit photon index is $\Gamma = 2.21^{+0.12}_{-0.18}$. The best-fit average torus column density is $\log(N_{\rm H,tor}) = 23.65^{+0.14}_{-0.05}$. The best-fit inclination angle is $\cos(\theta_{\rm inc}) = 0.25^{+0.52}_{-0.04}$, and the best-fit covering factor is $c_{\rm f,tor} < 0.25$.

C.2. Spectra of the 13 Sources

Unfolded NuSTAR, XMM-Newton, and Chandra spectra of different sources fitted with the `borus02` model when the inclination angle is left free to vary and the residuals between the data and best-fit predictions of the model are plotted in Figures C1 and C2. The NuSTAR data are plotted in blue, the XMM-Newton data are plotted in red, and the Chandra data are plotted in green. The best-fit model prediction is plotted as cyan solid lines. The single components of the model are plotted in black with different line styles, i.e., the absorbed intrinsic continuum with solid lines, the reflection component and Fe Kα line with dashed lines, and the scattered component, the `mekal` component, and Gaussian lines with dotted lines.

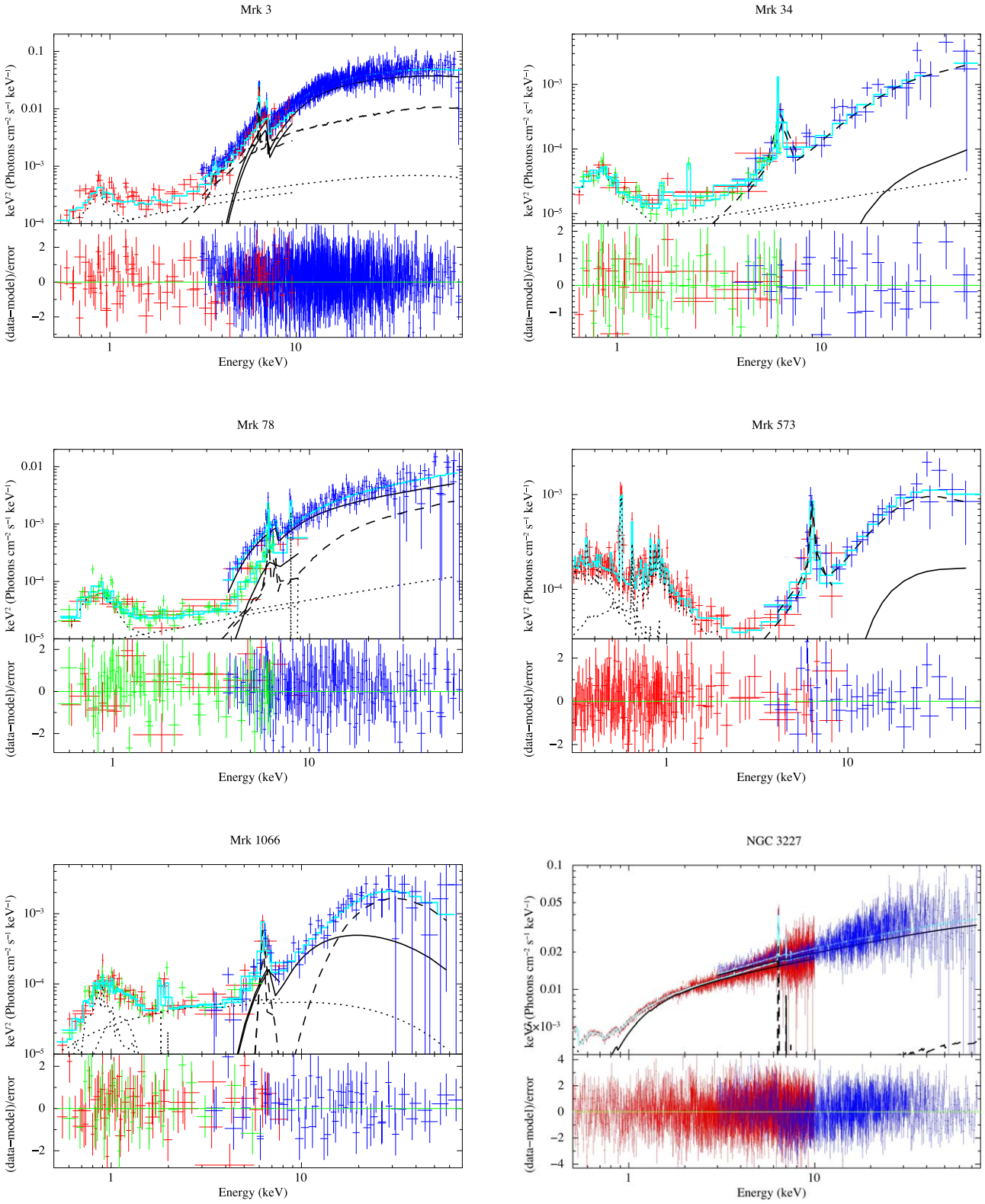

Figure C1. Unfolded NuSTAR, XMM-Newton, and Chandra spectra of different sources fitted with the `borus02` model when the inclination angle is left free to vary, and the residuals between the data and best-fit predictions of the model are shown. The NuSTAR data are plotted in blue, the XMM-Newton data are plotted in red, and the Chandra data are plotted in green. The best-fit model prediction is plotted by cyan solid lines. The single components of the model are plotted in black with different line styles, i.e., the absorbed intrinsic continuum with solid lines, the reflection component with dashed lines, and the scattered component, the `mekal` component, and emission lines with dotted lines.

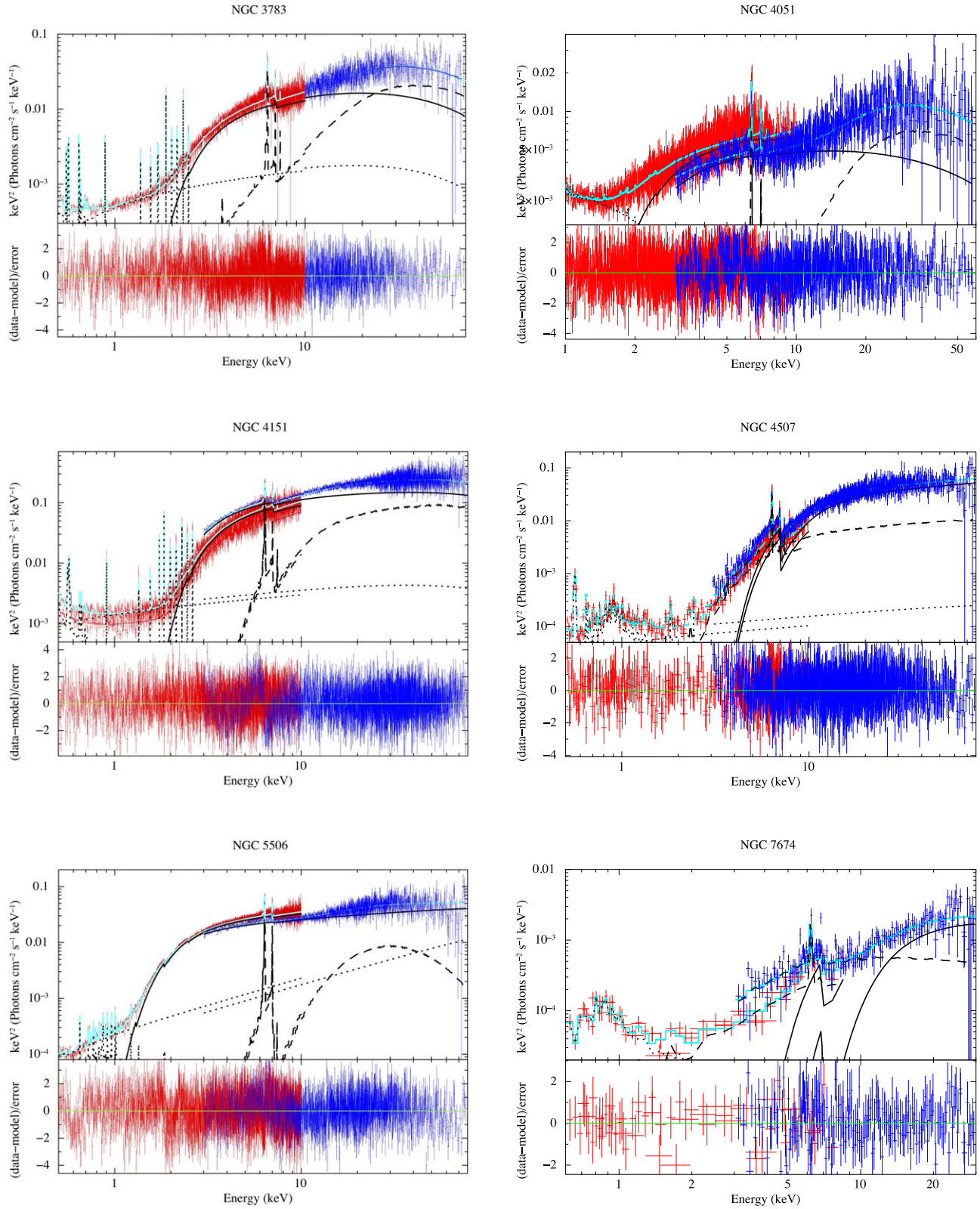

Figure C2. Unfolded NuSTAR, XMM-Newton, and Chandra spectra of different sources fitted with the `borus02` model when the inclination angle is left free to vary, and the residuals between the data and best-fit predictions of the model are shown. The NuSTAR data are plotted in blue, the XMM-Newton data are plotted in red, and the Chandra data are plotted in green. The best-fit model prediction is plotted by cyan solid lines. The single components of the model are plotted in black with different line styles, i.e., the absorbed intrinsic continuum with solid lines, the reflection component with dashed lines, and the scattered component, the `mekal` component, and emission lines with dotted lines.

ORCID iDs

X. Zhao https://orcid.org/0000-0002-7791-3671
S. Marchesi https://orcid.org/0000-0001-5544-0749
M. Ajello https://orcid.org/0000-0002-6584-1703
M. Baloković https://orcid.org/0000-0003-0476-6647
T. Fischer https://orcid.org/0000-0002-3365-8875

References

Alexander, D. M., Bauer, F. E., Brandt, W. N., et al. 2003, AJ, 126, 539
Almeida, C. R., Levenson, N. A., Espinosa, J. M. R., et al. 2009, ApJ, 702, 1127
Almeida, C. R., & Ricci, C. 2017, NatAs, 1, 679
Ananna, T. T., Treister, E., Urry, C. M., et al. 2019, ApJ, 871, 240
Anders, E., & Grevesse, N. 1989, GeCoA, 53, 197
Annuar, A., Gandhi, P., Alexander, D. M., et al. 2015, ApJ, 815, 36
Antonucci, R. 1993, ARA&A, 31, 473
Arévalo, P., Bauer, F. E., Puccetti, S., et al. 2014, ApJ, 791, 81
Arnaud, K. A. 1996, in ASP Conf. Ser. 101, Astronomical Data Analysis Software and Systems V, ed. G. H. Jacoby & J. Barnes (San Francisco, CA: ASP), 17
Baloković, M. 2017, PhD thesis, California Institute of Technology
Baloković, M., Brightman, M., Harrison, F. A., et al. 2018, ApJ, 854, 42
Baloković, M., Comastri, A., Harrison, F. A., et al. 2014, ApJ, 794, 111
Barthelmy, S. D., Barbier, L. M., Cummings, J. R., et al. 2005, SSRv, 120, 143
Bauer, F. E., Arévalo, P., Walton, D. J., et al. 2015, ApJ, 812, 116
Bauer, F. E., Brandt, W. N., Sambruna, R. M., et al. 2001, AJ, 122, 182
Beifiori, A., Courteau, S., Corsini, E. M., & Zhu, Y. 2012, MNRAS, 419, 2497
Beuchert, T., Markowitz, A. G., Dauser, T., et al. 2017, A&A, 603, A50
Bianchi, S., Maiolino, R., & Risaliti, G. 2012, AdAst, 2012, 17
Boorman, P. G., Gandhi, P., Baloković, M., et al. 2018, MNRAS, 477, 3775
Braito, V., Ballo, L., Reeves, J. N., et al. 2012, MNRAS, 428, 2516
Brightman, M., Baloković, M., Stern, D., et al. 2015, ApJ, 805, 41
Brightman, M., & Nandra, K. 2011, MNRAS, 413, 1206
de Marco, B., Adhikari, T. P., Ponti, G., et al. 2020, A&A, 634, A65
Denney, K. D., Watson, L. C., Peterson, B. M., et al. 2009, ApJ, 702, 1353
Fabian, A. C., Celotti, A., & Erlund, M. C. 2006, MNRAS: Lett., 373, L16
Fabian, A. C., Iwasawa, K., Reynolds, C. S., & Young, A. J. 2000, PASP, 112, 1145
Fabian, A. C., Vasudevan, R. V., Mushotzky, R. F., Winter, L. M., & Reynolds, C. S. 2009, MNRAS: Lett., 394, L89
Fischer, T. C., Crenshaw, D. M., Kraemer, S. B., & Schmitt, H. R. 2013, ApJS, 209, 1
Fruscione, A., McDowell, J. C., Allen, G. E., et al. 2006, Proc. SPIE, 6270, 62701V
Fürst, F., Müller, C., Madsen, K. K., et al. 2016, ApJ, 819, 150
Furui, S., Fukazawa, Y., Odaka, H., et al. 2016, ApJ, 818, 164
Gandhi, P., Annuar, A., Lansbury, G. B., et al. 2017, MNRAS, 467, 4606
Gandhi, P., & Fabian, A. C. 2003, MNRAS, 339, 1095
Gandhi, P., Lansbury, G. B., Alexander, D. M., et al. 2014, ApJ, 792, 117
Georgantopoulos, I., Comastri, A., Vignali, C., et al. 2013, A&A, 555, A43
Ghisellini, G., Haardt, F., & Matt, G. 1994, MNRAS, 267, 743
Gilli, R., Comastri, A., & Hasinger, G. 2007, A&A, 463, 79
Goulding, A. D., Alexander, D. M., Lehmer, B. D., & Mullaney, J. R. 2010, MNRAS, 406, 597
Harrison, F. A., Craig, W. W., Christensen, F. E., et al. 2013, ApJ, 770, 103
Hasinger, G. 2008, A&A, 490, 905
Heckman, T. M., & Best, P. N. 2014, ARA&A, 52, 589
Hickox, R. C., & Alexander, D. M. 2018, ARA&A, 56, 625
Ikeda, S., Awaki, H., & Terashima, Y. 2009, ApJ, 692, 608
Jansen, F., Lumb, D., Altieri, B., et al. 2001, A&A, 365, L1
Kalberla, P. M. W., Burton, W. B., Hartmann, Dap, et al. 2005, A&A, 440, 775
Kammoun, E. S., Miller, J. M., Zoghbi, A., et al. 2019, ApJ, 877, 102
Kawamuro, T., Ueda, Y., Tazaki, F., & Terashima, Y. 2013, ApJ, 770, 157
Kormendy, J., & Ho, L. C. 2013, ARA&A, 51, 511
Koss, M. J., Assef, R., Baloković, M., et al. 2016, ApJ, 825, 85
Koss, M. J., Romero-Cañizales, C., Baronchelli, L., et al. 2015, ApJ, 807, 149
Krolik, J. H., & Begelman, M. C. 1988, ApJ, 329, 702
Krolik, J. H., Madau, P., & Zycki, P. T. 1994, ApJL, 420, L57
la Caria, M.-M., Vignali, C., Lanzuisi, G., Gruppioni, C., & Pozzi, F. 2019, MNRAS, 487, 1662
LaMassa, S. M., Yaqoob, T., Ptak, A. F., et al. 2014, ApJ, 787, 61
Lawrence, A., & Elvis, M. 1982, ApJ, 256, 410
Leahy, D. A., & Creighton, J. 1993, MNRAS, 263, 314
Li, J., Xue, Y., Sun, M., et al. 2019, ApJ, 877, 5
Liu, Y., & Li, X. 2014, ApJ, 787, 52
Malkan, M. A., Gorjian, V., & Tam, R. 1998, ApJS, 117, 25
Mao, J., Mehdipour, M., Kaastra, J. S., et al. 2019, A&A, 621, A99
Marchesi, S., Ajello, M., Marcotulli, L., et al. 2018, ApJ, 854, 49
Marchesi, S., Ajello, M., Zhao, X., et al. 2019, ApJ, 872, 8
Marchesi, S., Tremblay, L., Ajello, M., et al. 2017, ApJ, 848, 53
Marinucci, A., Matt, G., Kara, E., et al. 2014, MNRAS, 440, 2347
Marinucci, A., Risaliti, G., Wang, J., et al. 2013, MNRAS, 429, 2581
Markowitz, A. G., Krumpe, M., & Nikutta, R. 2014, MNRAS, 439, 1403
Masini, A., Comastri, A., Hickox, R. C., et al. 2019, ApJ, 882, 83
Matt, G. 2002, MNRAS, 337, 147
Matt, G., & Fabian, A. C. 1994, MNRAS, 267, 187
Mehdipour, M., Kaastra, J. S., Kriss, G. A., et al. 2017, A&A, 607, A28
Merritt, D., & Ferrarese, L. 2001, MNRAS, 320, L30
Mewe, R., Gronenschild, E. H. B. M., & van den Oord, G. H. J. 1985, A&AS, 62, 197
Mizumoto, M., & Ebisawa, K. 2016, MNRAS, 466, 3259
Murphy, K. D., & Yaqoob, T. 2009, MNRAS, 397, 1549
Nandra, K. 2001, AdSpR, 28, 295
Nelson, C. H., & Whittle, M. 1995, ApJS, 99, 67
Nenkova, M., Sirocky, M. M., Ivezić, Ž., & Elitzur, M. 2008, ApJ, 685, 147
Netzer, H. 2015, ARA&A, 53, 365
Nicastro, F., Martocchia, A., & Matt, G. 2003, ApJL, 589, L13
Nikołajuk, M., Czerny, B., & Gurynowicz, P. 2009, MNRAS, 394, 2141
Noguchi, K., Terashima, Y., Ishino, Y., et al. 2010, ApJ, 711, 144
Onken, C. A., & Peterson, B. M. 2002, ApJ, 572, 746
Onken, C. A., Peterson, B. M., Dietrich, M., Robinson, A., & Salamanca, I. M. 2003, ApJ, 585, 121
Onken, C. A., Valluri, M., Peterson, B. M., et al. 2007, ApJ, 670, 105
Paltani, S., & Ricci, C. 2017, A&A, 607, A31
Puccetti, S., Comastri, A., Fiore, F., et al. 2014, ApJ, 793, 26
Reynolds, C. S. 1999, in ASP Conf. Ser. 161, High Energy Processes in Accreting Black Holes, ed. J. Poutanen & R. Svensson (San Francisco, CA: ASP), 178
Reynolds, C. S., & Nowak, M. A. 2003, PhR, 377, 389
Ricci, C., Bauer, F. E., Treister, E., et al. 2016, ApJ, 819, 4
Ricci, C., Trakhtenbrot, B., Koss, M. J., et al. 2017, Natur, 549, 488
Ricci, C., Ueda, Y., Paltani, S., et al. 2014, MNRAS, 441, 3622
Risaliti, G., Elvis, M., Fabbiano, G., Baldi, A., & Zezas, A. 2005, ApJL, 623, L93
Risaliti, G., Elvis, M., & Nicastro, F. 2002, ApJ, 571, 234
Shu, X. W., Yaqoob, T., & Wang, J. X. 2010, ApJS, 187, 581
Strüder, L., Briel, U., Dennerl, K., et al. 2001, A&A, 365, L18
Sun, S., Guainazzi, M., Ni, Q., et al. 2018, MNRAS, 478, 1900
Tanimoto, A., Ueda, Y., Odaka, H., et al. 2019, ApJ, 877, 95
Treister, E., Urry, C. M., & Virani, S. 2009, ApJ, 696, 110
Turner, M. J. L., Abbey, A., Arnaud, M., et al. 2001, A&A, 365, L27
Turner, T. J., Miller, L., Reeves, J. N., & Braito, V. 2017, MNRAS, 467, 3924
Ueda, Y., Akiyama, M., Hasinger, G., Miyaji, T., & Watson, M. G. 2014, ApJ, 786, 104
Urry, C. M., & Padovani, P. 1995, PASP, 107, 803
Ursini, F., Bassani, L., Panessa, F., et al. 2018, MNRAS, 474, 5684
Ursini, F., Marinucci, A., Matt, G., et al. 2015, MNRAS, 452, 3266
Ursini, F., Petrucci, P.-O., Matt, G., et al. 2016, MNRAS, 463, 382
Vasudevan, R. V., Fabian, A. C., Gandhi, P., Winter, L. M., & Mushotzky, R. F. 2010, MNRAS, 402, 1081
Verner, D., Ferland, G., Korista, K., & Yakovlev, D. 1996, ApJ, 465, 487
Walton, D. J., Nardini, E., Gallo, L. C., et al. 2019, MNRAS, 484, 2544
Winkler, C., Courvoisier, T. J.-L., di Cocco, G., et al. 2003, A&A, 411, L1
Woo, J.-H., & Urry, C. M. 2002, ApJ, 579, 530
Yaqoob, T. 2012, MNRAS, 423, 3360
Yaqoob, T., & Padmanabhan, U. 2004, ApJ, 604, 63
Yaqoob, T., Tatum, M. M., Scholtes, A., Gottlieb, A., & Turner, T. J. 2015, MNRAS, 454, 973
Zappacosta, L., Comastri, A., Civano, F., et al. 2018, ApJ, 854, 33
Zhao, X., Marchesi, S., & Ajello, M. 2019a, ApJ, 871, 182
Zhao, X., Marchesi, S., Ajello, M., et al. 2019b, ApJ, 870, 60